

Soft Tissue Material Properties and Viscoelastic Material Models for Finite Element Applications

by

John F. Riesterer

**A thesis submitted in partial fulfillment
of the requirements for the degree of
Master of Science
(Mechanical Engineering)
in the University of Michigan-Dearborn
2022**

Master's Thesis Committee:

**Professor Alan Argento, Chair
Associate Professor Joe Fujiou Lo
Associate Research Scientist Wonsuk Kim
Assistant Professor Guan (Gary) Xu, University of Michigan**

Dedication

This document is dedicated to Jenn; and to Leslie; thank you, both, for everything.

Table of Contents

Dedication	ii
List of Figures.....	v
List of Tables	vii
Abstract.....	viii
Chapter 1: Introduction	1
Chapter 2: Structure and Function of the Eye.....	2
2.1. Structure	2
2.2. Eye Disease	10
Chapter 3: Mechanical Modeling of Eye Structural Tissue.....	13
3.1. Models Overview	14
3.2. Available DYNA Material Models	17
Chapter 4: Mechanical Testing of Soft Tissues.....	22
4.1. Testing Procedures	24
4.1.1. Globe Perfusion Testing	24
4.1.2. Sample Mechanical Testing.....	27
4.2. Data Processing.....	31
4.3. Mechanical Testing Results	35
4.3.1. Discussion.....	38
Chapter 5: Optimization Using LS-OPT	43
5.1. Consistent Settings	43
5.2. Specific Model Settings	48
5.3. Other Topics.....	49
5.4. LS-OPT Parameter Results	51
Chapter 6: Finite Element Models	53
6.1. Models for Optimization and Validation	53
6.2. Development of Whole-Globe Models	58

6.3. Models of Whole-Globe Response to IOP.....	63
6.4. Validation Model Convergence Results.....	69
6.5. Whole-Globe Model Parameter Sweep Results.....	72
6.5.1. Discussion.....	73
6.5.2 Limitation of the FE Models	74
Chapter 7: Conclusions	77
Funding	77
Appendix 1	78
References	80

List of Figures

Figure 1: (a) Diagram of the structure of the eye. Source: https://www.nei.nih.gov/learn-about-eye-health/healthy-vision/how-eyes-work . (b) Diagram of the conventional aqueous outflow pathway.	2
Figure 2: Diagram of a large vein. Note that this diagram shows smooth muscle and valves within the vein, features not always present in smaller veins. Source: https://commons.wikimedia.org/wiki/File:Blood_vessels-en.svg	9
Figure 3: a. depicts the first cut splitting the two hemispheres of the globe, b. shows the ensuing cuts to flatten the hemisphere, c. depicts the approximate location for the excised dogbone on the flattened tissue region.	27
Figure 4: tensile elongation test data showing stress level through failure of sample.....	30
Figure 5: A sample raw data curve is shown along with 20-, 50-, and 100-point averages, highlighting the smoothing effect and lowering of the peak value induced by this process.	32
Figure 6: Showing the toe region based on the rolling Tangent Modulus vs. Stress calculation. This method predicts the end of the toe of this sample around 0.02 MPa.	33
Figure 7: Representative 0.5 mm/min (a.) and 100 mm/min (b.) stress-time relaxation curves. The lower rate samples relax much less per unit time than the higher rate samples over the same time period.	36
Figure 8: Stress-log(time) charts of the average high and low rate sample data. Note that the low rate data Y axis is truncated to better highlight the curve shape.	37
Figure 9: The average material tensile data is plotted against the SECFORC-Computed Stress and the DYNA Output Stress. The method by which LS-DYNA outputs the stress is clearly important in the experimental design.....	50
Figure 10: Dogbone FE Model for applying displacement boundary condition orthogonally to the surface of one end while fixing the other end. Two different mesh densities are shown.	57
Figure 11: a flat segment of tissue model with applied wall pressures as boundary conditions (arrows).....	59
Figure 12: A series of "forcing element" FE models meant to investigate methods of applying IOP loading to the internal surface of a globe segment.....	60
Figure 13: Vein-in-tissue models with increasing mesh densities. The thin vein elements limit the timestep size of the FE Model.....	62
Figure 14: Quarter and Full Hoop FE Models exploring the application of IOP in a radially balanced manner.	63
Figure 15: Eighth Sphere FE Models of increasing density. Note that from c. to d. only a small central region of elements was further reduced in size, with the hopes of keeping computational time under control.	64

Figure 16: method for linking hex elements of different sizes using only valid 3D element shapes.....	65
Figure 17: highlighting the region surrounding the vein structure, using the radial element orientation from previous chunk models to surround the vein.	66
Figure 18: Sphere segment chunk model, a. without vein structure and b. with vein structure..	66
Figure 19: Plot of percent difference between SIDR load and conventional load at $t = 0$ s. The difference increased for each higher SIDR load applied, but was still just under 2% difference for the third preload to 14.5 mmHg.....	68
Figure 20: a., b., and c. show the convergent behavior of the dogbone models with increasing mesh density at different times, while d. demonstrates that the values are not converging to the predicted LS-OPT value.	69
Figure 21: The value of the stress at $t = 25$ s can be seen to grow closer and closer to the LS-OPT predicted value as the HG coefficient drops to zero. However, it never reaches the predicted value.....	70
Figure 22: Convergence of maximum principal stress value in eighth sphere model with increasing mesh density.	70
Figure 23: Tissue chunk model strains for a. the vein, b. the outer surface of the globe model, and c. the layer of elements surrounding the vein. In a., the “Structural Vein strain” is a measure of the change in diameter of the vein, meant to reflect the amount of deformation the vein as a whole experiences during IOP loading	72

List of Tables

Table 1. Stress at 8% strain and Tangent Modulus from Linear Region (mean \pm SE)

Table 2. 5 Parameter and 7 parameter model coefficients (mean \pm SE)

Table 3. MAT 092 Material Parameters

Table 4. MAT 176 Best-Fit Parameter Sets

Abstract

This thesis treats mechanical testing and modeling of eye tissue using the porcine eye as the representative model. The goal of the work is to combine finite element (FE) techniques and material data to generate an improved understanding of the mechanical behaviors of sclera with a reliable FE model.

The mechanical properties of porcine sclera dogbone-shaped samples are studied in tension at various loading rates. A randomly selected group of samples is treated with a chemical cross-linking agent (genipin) to artificially stiffen their mechanical response. Response data is collected during both loading and relaxation of tissue samples at three quasi-static strain rates, 0.0006/s, 0.013/s, and 0.13/s. Measures of the tissue responses are then extracted and used to investigate average material property differences in treated and untreated tissue samples.

The mechanical properties of porcine sclera are further investigated using whole, trimmed globes in a specialized testing system. The whole globes are perfused using an aqueous humor analog to generate loading conditions approximating those *in vivo*.

The collected mechanical data is used to inform a series of material models in FE simulations of the mechanical tests. The method of generating material parameters is outlined, and a series of parameter sets are presented for each strain rate and each material treatment. The optimized parameter results are compared to the mechanical testing data using FE models of the mechanical testing process. Convergence of different FE models with increasing mesh density is demonstrated. Finally, FE models of the globe inflation process are informed with the optimized material model parameter sets and loaded to simulate the response of the globe under the action of intraocular pressure.

Primary findings demonstrate a significant difference in material properties characterizing loading and relaxation of the genipin-treated and untreated sample groups. The parameter sets generated for each average group of samples are shown to fit the data well. Simulated globe inflation strain results were found to be greater in the untreated case than in the treated case. The

untreated model strains compare well to photoacoustic image-measured strains and to strains reported in literature for similar processes.

Chapter 1: Introduction

The presence of the light of the sun has wielded a strong influence upon almost every living organism on our planet for billions of years. Whether visual organs evolved many times independently of one another [1], or whether molecular remnants in all visual organs indicate the presence of a single genetic ancestor of biological sight [2], the existence of eyesight today is a remarkable achievement. Charles Darwin wrestled with the topic in his pioneering work *On the origin of species*, devoting a section called “Organs of extreme perfection and complication” to the challenge of explaining visual organs [3]. Regardless of how it happened, the eye is an incredibly complex organ that performs its task of focusing light into the retinal tissues to allow us to process the world around us in striking detail [4].

There is room to understand more about every aspect of the eye, from its structure and function to its tendencies towards disease and its molecular components. In seeking to understand our eyes, researchers often use porcine eyes as an animal model of the human eye [5]. Despite some physical differences, like the vastly different morphology of certain fluid drainage tracts [6], porcine globes largely act as an effective model for their human counterparts. Some common diseases of the eye, such as glaucomas, are still less understood than we would like, and they continue to affect tens of millions of people around the world today [7]. Further, the small scale of fluid structures within the eye makes the study of its physical characteristics more challenging than other, larger soft tissue structures. This work seeks to expand upon that knowledge base by combining mechanical testing results and an optimized finite element mechanical model to improve the prediction of tissue stresses and strains within the sclera as a response to intraocular pressure (IOP).

Chapter 2: Structure and Function of the Eye

2.1. Structure

To better understand the driving forces of eye disease, and especially the glaucomas, it is important to look at the structure and function of normal eye tissue. The focus of this summary will remain on the sclera and its related structures, but some discussion will be made of all the eye's basic structures. To start, the eye is a complex organ (Figure 1(a)) with many parts working together to enable vision. The eye is encapsulated by fat and connective tissue within the orbit, and this protects the eye and holds it in place. In the human eye, there are six ocular muscles connecting the orbit and the eye that control positioning of the eye for purposes of sight [8]. There is a seventh muscle that controls the eyelid position [9]. The eye can be thought of as a

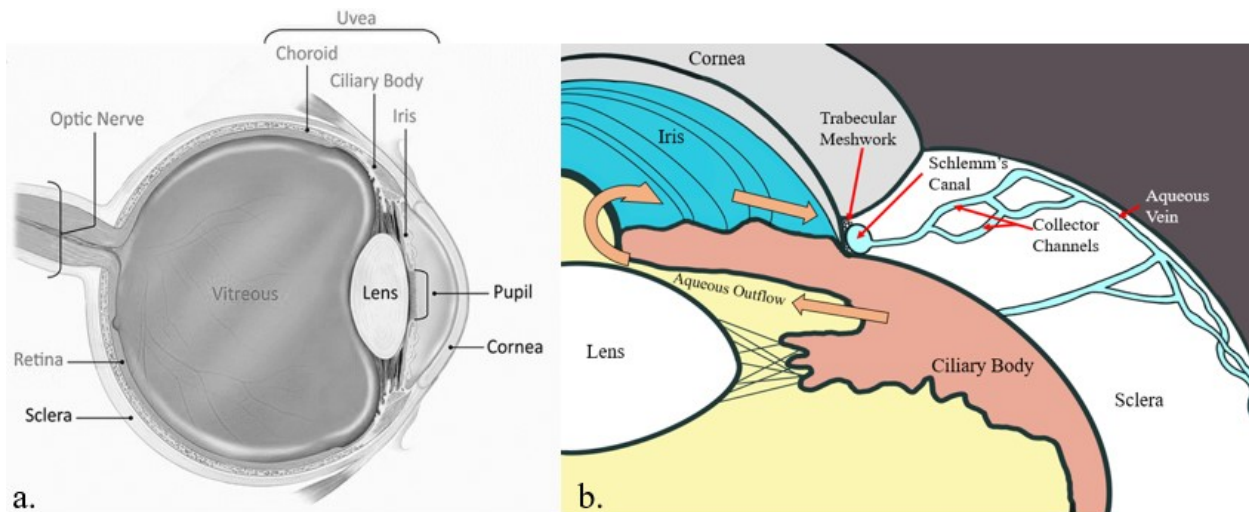


Figure 1: (a) Diagram of the structure of the eye. Source: <https://www.nei.nih.gov/learn-about-eye-health/healthy-vision/how-eyes-work>. (b) Diagram of the conventional aqueous outflow pathway.

body with multiple layers. These layers are then filled with three distinct, transparent bodies that work together to focus light. If we think of the eye like a balloon, then the three layers surrounding the transparent structures can be considered like the latex of an inflated balloon. There is the outer shell, which consists of the cornea and the sclera. Inside of this outer shell are structures that include the iris, choroid, and ciliary body. Those objects support and enable

vision. Then the inner-most layer is the retina. This is the structure that receives the focused light transmitted by the transparent structures. The transparent structures are the lens, the aqueous humor (or fluid), and the vitreous fluid [10]. The aqueous is found in the anterior chamber, in front of the lens. The lens sits between the aqueous-containing anterior chamber and the vitreous-filled posterior chamber, mounted to the ciliary body by a ligament called the zonule [10]. The vitreous chamber, filled with vitreous, occupies the remaining volume of the eye behind the lens.

Cornea

The cornea is the most forward part of the eye, and it is transparent so that light can pass through and move towards the lens. It is completely avascular, and so the aqueous humor is the source of nutrients for the cells of the cornea [11]. The cornea is heavily innervated, in fact the most innervated structure of the body, and these nerves are used for sensing temperature, touch, and pain. The inputs sensed by the corneal nerves are then used by the body to control things like blinking and tear secretion. Before the discovery of nerves in the cornea by Friedrich Schlemm in 1831, it was thought to be without any innervation [12]. There is an optic zone of approx. 4 mm diameter located in the center of the cornea, and this is surrounded by a peripheral region, comprised of the remaining cornea tissue. A region of tissue called the limbus connects the peripheral cornea to the sclera. The limbus contains the aqueous outflow channels [13]. There are five distinct layers of the human cornea. The epithelium and endothelium are the outermost and innermost layers of the tissue. Moving inward from the epithelium towards the endothelium, there is the Bowman's layer, the stroma, and the Descemet's membrane. The stroma is approx. 500 μm thick, and it is made of many collagen lamellae that are arranged so that light can pass through the cornea [10].

Sclera

The sclera, which makes up most of the external shell of the eye, is also the primary load-bearing structure for the eye. It is a composite structure, made of mainly type I and type III collagen suspended in a matrix of hydrated proteoglycans, cells, and elastin fibers. The collagen in the sclera is over 90% type I, with less than 5% of the collagen being type III, and the remaining percentage being composed of other types of collagen. The collagen fibrils of the sclera, like

those of the cornea, are organized into lamellae within the sclera. However, unlike in the cornea, the spacing between the scleral lamellae is irregular, and the fibrils are oriented over a range of angles and distributed without a sole obvious governing motif [14]. The collagen lamellae are strongly anisotropic, resisting axial forces well, and providing little resistance to applied forces transverse to the axis of the lamellae. Collagen fibrils are very stiff, and the surrounding matrix is relatively soft. The prevailing theory of collagen behavior under tensile loading is that the fibrils are wavy and relatively disorganized when they are not loaded. Once they are mechanically loaded, they first un-crimp and align, then progressively carry more force as they become more aligned [14]. This is used to explain the classic “J-shaped” stress-strain curve of directional collagenous tissues. Single collagen fibrils are cross-linked to one another by the matrix proteoglycans decorin and biglycan. These proteoglycans have glycosaminoglycan (GAG) side chains that connect adjacent collagen fibers [15]. These GAGs retain water due to their negative charge, and are therefore thought to increase the structural stability of the sclera. Changes to the GAGs can influence the properties of eye tissue, and it is known that the amount of biglycan and decorin both decrease after the fourth decade of life [16].

The orientation and distribution of collagen lamellae within the sclera is generally disordered, with some regions of very directional lamellae. The collagen fibrils of the perilimbal and peripapillary regions are highly anisotropic, oriented circumferentially around the cornea and optic nerve head (ONH). These regions are postulated to contribute to supporting the difference in curvature between the sclera and cornea, and supporting the critical ONH structure, respectively. Moving backwards from the limbus region, there are found four regions of highly aligned fibrils at the cardinal direction points of the anterior hemisphere of the sclera. These aligned regions of collagen coincide with the insertions of the four recti muscles of the eye, and it is sensible to suggest that these regions exist to reinforce those muscular insertions. There is another patch of highly aligned collagen found on the posterior sclera whose location and orientation correspond well to possibly resisting the forces of the oblique eye muscles [17].

Vitreous and Aqueous Humors

The vitreous and aqueous humors are fluids found only in the eye. They are both clear liquids, but the two have different viscous characteristics and are physically separated by the lens *in vivo*.

The vitreous is a shear-resistant fluid with a viscosity two to four times greater than that of water, and it fills the volume behind the lens. It clings to the surrounding retina. The vitreous helps maintain the shape of the eye globe while also allowing for light to pass from the lens to the retinal tissue. It is a network of various forms of collagen, highly cross-linked. The dominant collagen form is type II, but types V, IX and XI are also present. One of the aforementioned GAGs, hyaluronic acid, is found throughout the vitreous humor. Cells within the vitreous receive their nutrition from the vessels of the retina and the ciliary body [18].

The aqueous humor is different from the vitreous in that it has a low viscosity similar to that of water [19]. In a study concerning the viscosity of aqueous in humans with PAOG, cataract, and pseudoexfoliation syndrome, a range of viscosities from 0.71-0.72 mPa·s were measured [20]. For reference, the dynamic viscosity of water at 37°C is approx. 0.7 mPa·s. The data for all three disease groups was found to be significantly different from that of water, but at a level that is not considered clinically relevant.

The flow of aqueous humor is determined by the difference between the rate of aqueous generation in the ciliary body and resistance to aqueous outflow from the anterior chamber by the aqueous outflow system [21].

The aqueous fluid has several important functions in the anterior chamber. Just as the vitreous acts to hold the shape of the vitreous chamber, the aqueous humor preserves the shape of the cornea. The aqueous also provides nutrients to the cornea, a critical function considering the avascular cornea has little other way to obtain nutrients. Aqueous also removes waste products from the eye. The aqueous is produced in the ciliary body, and most of it flows through the anterior chamber and exits the eye via the primary outflow system (Figure 1(b)), through the trabecular meshwork and into Schlemm's canal, then into the episcleral veins [22]. The remaining portion, anywhere from 5 to 35% of the aqueous, drains through the so-called uveoscleral pathway [23]. The uveoscleral pathway is comprised of channels external to the primary outflow pathway, along with the ability of aqueous to diffuse directly into tissues. Aqueous can flow between the bundles of the ciliary muscle, through perivascular spaces, and also within the suprachoroidal space, through channels that are attached to the intrascleral venous

plexus. Further, since aqueous humor is over 99% water, and most of the constituent molecules are relatively small, much of the aqueous can pass through the sclera, with or without the presence of scleral pores [24]. A study of uveoscleral outflow in monkeys found that the outflow was decreased during contraction of the ciliary muscle, and also increased by the muscle's relaxation [25]. There is no epithelium between the ciliary muscle and anterior chamber, further confirming the ability of aqueous to flow out through the ciliary muscle [25].

Trabecular Meshwork

The trabecular meshwork (TM) is a structure found in the iridocorneal angle that exists between the anterior chamber and Schlemm's canal. It is made up of three distinct layers, the uveal meshwork, the corneoscleral meshwork, and the juxtacanalicular tissue (JCT). The TM is made of many scattered pillar- or beam-type structures of connective tissue with cores of collagen and elastic fibers [26]. The elastic fibers of these pillars contain very little elastin, and those elastic microfibrils are embedded in an electron-dense matrix material that remains poorly understood [27]. These pillars cross and twist around one another to form the porous meshwork. Starting with the layer most distal to the Schlemm's canal, the uveal meshwork is made of one to three layers of connective tissue beams. Following that inward, the corneoscleral mesh is made up of more layers, as many as 15. The pillars of the corneoscleral meshwork are much thicker. After the corneoscleral mesh, there is found the JCT, which is made of loose connective tissue. Several layers of dispersed cells can be found here, embedded in a unique extracellular matrix (ECM) [26]. This ECM is critical in modulating the outflow resistance of the anterior chamber. It has been found that cells within the ECM are sensitive to stretch, and they will respond to increases in the distortion of the ECM by releasing enzymes that will degrade the ECM to lower resistance. Also noted is that the mRNA for ECM-expressing genes is present in relatively high amounts within the trabecular meshwork, implying that the remodeling of ECM within the JCT is a near-constant process of degradation and replacement [28].

It can be demonstrated that the trabecular meshwork is influenced by the muscles of the ciliary body. These muscle bundles attach to the scleral spur, and when contracted they open the trabecular space further. There are also a second family of contractile cells within the scleral spur which are connected to scleral spur elastic fibers. Those fibers are then continuous with those in

the JCT and trabecular mesh. It is likely that these contractile cells change the shape of the outflow pathways through the trabecular mesh and JCT. They are mostly oriented in a circumferential direction, and this suggests that these cells can act to oppose the muscle bundles of the ciliary body [26].

Aqueous Outflow Veins

Much emphasis has been placed to this point on studying the behavior and interactions of the trabecular meshwork with the aqueous fluid and the anterior chamber. However, there is less research performed on the aqueous drainage structure found distal to Schlemm's canal. The distal outflow system consists of the drainage structures that extend back towards the ONH from Schlemm's canal. There are small veins known as collector channels (CCs) that allow aqueous to flow away from the anterior chamber. From the CCs, aqueous humor can flow through one of two pathways. It can pass into the aqueous venous plexus network, consisting of a deep, mid-limbal, and perilimbal venous plexus. From here it drains into veins within the sclera. Otherwise, it can flow outward from the Schlemm's canal by the aqueous veins which connect directly to the episcleral veins [29].

Collector Channels

These CCs dot the distal wall of Schlemm's canal and are broadly grouped into two categories. There are so-called "simple" orifices, oval-shaped openings that are completely open and show a thin layer of endothelium within the channel and surrounding its lip. Some simple channels have thicker endothelial layers around the lip. Other simple channels seem to have a lip around half of the opening, with a divot on the opposite side that have been collectively postulated to act as a funneling device [30]. There are also "complex" CC openings in the outer wall of Schlemm's canal. These complex orifices can be similarly shaped to simple CC openings, or they can be more elongated, and if elongated they will often be spanned by tissue bridges that are assumed to be necessary to preserve vein patency. Along with tissue bridges, many complex openings are also covered by tissue structures that resemble flaps, which attach to the Schlemm's canal endothelium only along one side such that the other edge is free to move [30]. It has been shown that changes in IOP can cause changes in the shape of these flap-like structures, implying that they do indeed function as gates for some of the complex CC openings [31].

Aqueous Venous Plexus

The aqueous venous plexus (AVP) refers to a chaotic and tortuous group of veins found distal to the collector channels. They can be seen branching off from the collector channels in adult human eyes [32]. As mentioned above, they are divided into three sub-groups, known as the deep, midlimbal, and perilimbal intrascleral venous plexus (DIVP, MLIP, PIVP, respectively). These names simply refer to the depth of the respective venous plexuses. The intrascleral plexuses, as they are collectively termed, are made of a series of branching and interlinked venules that can be from 10-50 μm in diameter [33]. The DIVP has been measured as anywhere from 250-320 μm from the surface of the sclera in a study where only two of the three intrascleral plexuses were resolved [34]. In the same study, the PIVP was measured at between 95-133 μm deep into the sclera [34]. The MLIP has been imaged using OCT angiography, and was noted to be densely organized close to the limbus region, while thinning considerably as the images progress away from the limbus [35]. Taken together, these three levels of venous plexuses are a chaotic mass of aqueous drainage veins that penetrate the sclera at all depths. The venous plexuses drain posteriorly to several larger radial veins that in turn connect to the larger episcleral veins, a drainage pathway for both aqueous and blood [33].

Aqueous Veins/ Ascher's Aqueous Veins

The aqueous veins, sometimes also called the aqueous veins of Ascher, connect the CCs and the episcleral drainage veins directly, without passage through the tortuous venous plexus system. The aqueous veins *in vivo* contain only aqueous humor at their origin, but they do connect with the blood and aqueous draining episcleral veins. The mixing of blood and aqueous in the distal aqueous veins can be used to measure or describe the magnitude of changes in IOP, blood further up the aqueous veins can indicate a lower IOP, and higher IOP can cause clear aqueous fluid to push further down the aqueous veins. Aqueous veins vary from 20-100 μm , and are compositionally very similar to episcleral and conjunctival veins when examined through histology [33].

Perivascular Tethering

To discuss the relationship between aqueous outflow pathways and their surrounding tissue, it is

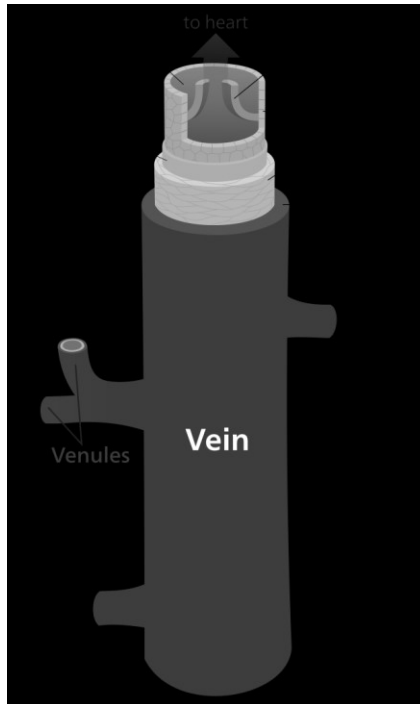


Figure 2: Diagram of a large vein. Note that this diagram shows smooth muscle and valves within the vein, features not always present in smaller veins. Source: https://commons.wikimedia.org/wiki/File:Blood_vessels-en.svg

necessary to have some understanding of the connections between the two surfaces. In general, a vein (see Figure 2) is made up of two to three layers, and they are called the intima, media, and adventitia (or externa). The intima is the innermost layer, and for smaller vessels is just the vein endothelium. The media of a vein is made of smooth muscle cells and a small amount of elastic tissue, along with distributed bundles of elastic and collagenous fibrils. There is usually a layer of elastin that divides the media and externa. The vein adventitia is generally thick, relative to the other layers, and contains predominantly collagen. The elastin-collagen ratio of an average vein is approx. 1:3 [36]. The collagen of the adventitial layer of veins and arteries is known to facilitate vein anchoring to surrounding tissue structures [37]. However, the venules and capillaries of the aqueous outflow system are some of the smallest veins in the body. At these scales, some

of the three layers are much thinner or altogether absent. There is very little published information to be found on the tethering of aqueous veins, episcleral veins, CCs, or any of the venous plexuses to their surrounding tissues. It is known, for example, that the capillaries of the heart are abundantly tethered to surrounding muscle cells [38]. In 1971, MJ Hogan's histological textbook stated that they had been unable to find a physical connection between the CCs and their surrounding tissue [39]. Hogan suggests that the CCs merely exist to increase the Schlemm's canal outer wall surface area, although the presence of a wall that separates the CC endothelium from the trabecular space is also described. This "wall" could be referring to a rudimentary vein wall. The same work also states that the connective tissue of Schlemm's canal does continue out along the external wall of the CCs as a very thin layer, and that there are sparsely distributed muscle cells within this layer. The adventitia was observed to disappear from

these CCs as they meet with the DIVP [39]. A 1982 text by FA Jakobiec echoes this observation, saying that an “extremely attenuated” continuation of the connective tissue surrounding Schlemm’s canal exists around the CCs [40].

It is likely that aqueous veins lack a muscle cell layer and are generally very histologically simple structures, with its largest drainage vessel (Schlemm’s canal) resting on the surrounding sclera and epithelial vessels connected to their basal layer by pericytes [41]. Veins in this work are meant to represent those smaller vessels, and are modeled as continuous with the wall, with a single set of nodes composing both the outer surface of the vein and the inner surface of the tissue wall. One instance of the whole-globe model used a single soft layer of elements between sclera and vein to represent their connection to the sclera.

2.2. Eye Disease

Glaucoma

Glaucoma is a word for a range of conditions that are primarily characterized by the progressive decay of retinal ganglion cells [42, 43]. The result of this decay is progressive vision loss. The glaucomas are generally associated with chronic, elevated intra-ocular pressure (IOP). In its early stages, glaucoma is not symptomatic, and this can allow the disease to progress unchecked until it has already caused significant loss of the patient’s visual field [44]. Elevated IOP is known to be associated with disease progression, but other risk factors include old age, black race, and use of topical or systemic corticosteroids [43]. Glaucoma is treatable through management of IOP, either by surgical or chemical means. However, the lowering of high IOP does not always halt disease progression, and the reasons for this are unknown [45]. There are two broad categories of glaucoma, open-angle glaucoma and angle closure glaucoma. These can be further classified as either primary, if the glaucoma has no apparent cause, or secondary, if the glaucoma is caused by another factor, such as trauma to the eye. Primary Open-Angle Glaucoma (POAG) is generally more prevalent than the other types of glaucoma, although there is some variance amongst different races and populations. For example, Primary Angle Closure Glaucoma (PACG) is much more prevalent in Asia (approx. 15.47 million cases in 2013) than it is in North America (approx. 0.39 million cases in 2013) [46]. Angle closure glaucoma is characterized by the iris’ occlusion of the trabecular meshwork, and is defined so that at least $\frac{3}{4}$ of the iridocorneal angle must be

blocked for a positive diagnosis. Open-angle glaucoma is when there exists increased outflow resistance without physical blockage of the iridocorneal angle by the iris. This increased outflow resistance is thought to be associated with changes in the trabecular meshwork [43]. One potential explanation for the increased resistance of POAG is a protein called myocilin. Mutations of the MYOC gene, which encodes for myocilin, are known to be associated with juvenile- and adult-onset POAG. Myocilin is expressed in many structures of the eye, including the sclera and trabecular meshwork. It can be found in many organs besides the eye. It is also secreted in the aqueous humor [47]. The secretion of myocilin in the trabecular meshwork can be triggered through corticosteroid application [48]. Studies seeking to show increased myocilin secretion acts to increase IOP have been inconclusive, with some identifying a positive correlation between increased myocilin and raised IOP, and others finding the exact opposite. It has been postulated that increased myocilin presence in eye structures could be an effect of increased IOP, and not a cause. The purpose of myocilin in the physical structures of the eye is still poorly understood, leading to further challenges in understanding its correlation with glaucoma [49].

Age-Related Macular Degeneration

The focus of this work is the sclera and its composite structure with some attention also paid to the small aqueous veins. Age-Related Macular Degeneration (AMD) will not receive significant treatment in this document, as it is not a disease that is expected to be related to those topics. However, with its general relevance as a common disorder of the eye, it is necessary to give a brief summary of the condition. AMD is one of the leading causes of vision loss in older people around the world [50, 51]. The degeneration of the macula, or central region of the retina, is caused by the excessive deposition of aggregates called drusen [51]. Though they are naturally found in small quantities as an effect of aging, the accumulation of a large amount of drusen can lead to the retinal damage and progressive vision loss characterizing the disorder [52]. The development of AMD is a complex process, with current research identifying a host of genetic, lifestyle and demographic risk factors [53]. Some of these risk factors include smoking, obesity and dietary makeup, and race. Gender may or may not have an effect on AMD rates [54]. Some research has been performed to identify the role of the sclera in the development of AMD. A

classic study found an increased coefficient of scleral rigidity of AMD patients vs. control patients in 1989 [55], with a later study identifying increased scleral rigidity in patients with neovascular AMD in 2006 [56].

Chapter 3: Mechanical Modeling of Eye Structural Tissue

With the preceding sections outlining the structure and function of eye tissues and some of its characteristic properties, there is sufficient context to begin discussion of the many different ways in which eye tissue can be and has been modeled. The collagen fibrils of the cornea and sclera are aggregated into lamellae, which are embedded in a hydrated proteoglycan matrix [57]. It is therefore sensible to model the sclera by describing its stress response as a matrix-fiber composite. Many efforts over the past 20 years to model the cornea and the sclera have taken this approach [14, 57-60]. Other models have found it sufficient to apply macroscopic-level measured properties to the entire sclera and/or cornea, instead of describing the matrix and fiber responses separately [61-63]. It is not inherently wrong to choose either method, and good results can be achieved in either case. By modeling the sclera with respect to its microstructural composition, there could be better physical agreement of the model with the real-world behavior of the tissue. However, using such methods can result in computationally expensive models that take a long amount of time to generate useful data.

Soft Tissue Material Properties

It is known that collagenous soft tissues are [64] anisotropic, highly deformable, rate-dependent, and viscoelastic. Soft tissue anisotropy is a result of the directional alignment of collagen fibrils, which also give rise to the characteristic stiffening stress-strain behavior through their gradual recruitment during tissue loading [65]. These types of soft tissues are highly deformable due to the interactions between collagen and the ground substance material in which the collagen fibrils are embedded. The anisotropy and high deformability of soft tissue make it a natural candidate for description with a strain energy density function, known as a hyperelastic material modeling approach [66]. Soft tissues tend to be significantly rate dependent [67, 68], and this is thought to be an effect of micro- and macro-structural interactions between the collagen and ground substance [69]. A viscoelastic material displays properties of both viscous and elastic materials. These materials will undergo time dependent behavior [70]. Viscoelasticity has been

demonstrated in collagen fibrils, although the results suggested that the viscoelastic behavior of soft tissue is largely caused by the components of the embedding ground substance [71]. With these complex behaviors known and understood to varying degrees, it is necessary that any testing of soft tissue is designed to explore these behaviors, and that any modeling of collagenous soft tissues uses mathematical representations of hyperelasticity and/or nonlinear viscoelasticity.

3.1. Models Overview

Linear Elastic, Isotropic

Arguably the simplest way to describe the material composition of the sclera is by using a linear elastic, isotropic material model. This is what was used by Norman et al. when simulating whole globe shells to understand the effects on the ONH. This group was able to use such a model to see that scleral thickness at the peripapillary tissue of the sclera had a strong effect on the induced strains across the ONH and lamina cribrosa [62]. The obvious advantage of such a model would be its simplicity, allowing for presumably rapid simulation of the desired geometries. A similarly obvious drawback is that eye tissue has been well-documented as a viscoelastic material. Using linear elastic theory would surely result in misrepresenting some of the stresses and strains.

Viscoelastic

A viscoelastic model instead of a linear elastic model for eye tissue offers a more complete description of sclera constitutive behavior. Two of the simpler models that can be used for this purpose include Maxwell and Kelvin-Voigt models. These models are combinations of linear spring and damper elements that work together to mimic viscoelastic behaviors [72]. A Kelvin-Voigt model was used to simulate an applanation test of a cornea and was found to perform well, producing good agreement with the experimental data. A Maxwell model was not used, as it is not bound by a spring in parallel, and so it can creep indefinitely [73]. A similar model uses linear spring elements that engage at progressively more strain, creating the characteristic “J-shape” of soft tissue loading curves with 4 or more spring elements [74]. A study of sheep eye collagen microstructure used this model to describe how heterogeneous levels of collagen fiber crimping in the peripapillary sclera could produce this characteristic soft tissue loading behavior [75]. One drawback of using this model is that it requires damper elements and parallel branches

to generate relaxation behavior. It is also rather simplistic, equating the function of the ligaments of the body to some finite number of spring and damper elements.

He et al. were able to characterize the mechanical behavior of sclera using a viscoelastic and isotropic model, so that their results were able to describe age-related macular degeneration (AMD)-affected posterior sclera tissue as isotropic, despite finding healthy posterior sclera tissue to be anisotropic [76]. They also reported good relaxation behavior capture by this model.

Despite knowledge that eye tissue is anisotropic, this model does offer a good example of a case in which eye tissue can be modeled as isotropic (in AMD-affected tissues).

Poroelastic

There is also the poroelastic model for describing tissue behavior and fluid-tissue interactions. Poroelasticity concerns a material that is porous and whose pores are filled with fluid. Then, the flow of the fluid through and out of the pores contributes to the tissue response and alters the mechanical behavior. The viscous behavior is provided by the fluid as it flows through or out of the pores due to loading conditions [77]. Further, the stress response of the material is a combination of the responses of the solid, the fluid, and the pore spaces. This model is useful due to its treatment of the physical nature of porous materials to describe the stress evolution. The flow of fluid in a porous media is a straightforward physical explanation for a complex problem like stress relaxation. One possible drawback to this particular model is that despite its ability to describe the contribution of the fluid, pores, and solid to the total stress condition, it does not provide a tool for looking at specific pore arrangements. This works well for many macroscopic applications, but does not allow for the microstructural analysis of a material. Another problem that can arise in applying such a material model is the instability of the boundaries of the solution to a finite element poroelastic loading problem at high rate. Specifically, the fluid pressure can begin to behave unpredictably as the tissue is quickly loaded [78].

Fiber-Matrix Composite

Modeling the sclera behavior as a composite of stiff fibers embedded in a softer matrix material is likely the most computationally expensive way of describing the tissue. However, it is generally effective at capturing macro-scale behaviors of the sclera. Coudrillier et al. used a

digital image correlation (DIC) system to image displacements of the posterior sclera surrounding the ONH, then used that displacement data to assign material properties for the region [14]. The same research group used the same form of constitutive model to ascribe quantitative properties to anterior eye tissue structures through collected strain map data. Both the material properties associated with matrix and those associated with collagen were increased for glaucomatous eyes as compared to control eyes [57]. Another study by Pinsky et al. used a similar strain energy function approach to assign properties to both the cornea and the sclera in a model of the response of perilimbal tissues to a small tunnel incision in the sclera [58]. Grytz et al. applied a more complex model that incorporated collagen uncrimping and relative collagen fibril size, finding that there was a large distribution of material parameters needed to fit the collected data, but that this model estimated a value for the collagen fibril elastic modulus in good agreement with a previous work of theirs [59]. More recently, Wang et al. were able to demonstrate that interweaving of collagen fibrils resulted in a higher predicted elastic modulus for the fibrils, and they stated that this implied a woven collagen network could have great influence on the overarching mechanical properties of the sclera [60]. The strong influence of collagen fibril properties on the macroscopic tissue behavior seen in several of these cases indicates that an understanding of collagen behavior is likely critical to improving sclera and other collagenous soft tissue model accuracy, although sometimes an overly specific model can be too sensitive to slight variations of parameter values.

Quasi-Linear Viscoelasticity (QLV)

Another viscoelastic model that explores the relationship between viscous and elastic behaviors is the Quasi-Linear Viscoelastic (QLV) model developed by YC Fung and published in 1997 [36]. This model decomposes the stress behavior over time into a function of time, $G(t)$ (the relaxation function), and a function of stretch, $T^{(e)}(\lambda)$. A result of this division of the stress response, is that the problem allows for the separation of the loading and relaxation behavior of the tissue. A prony series is commonly used to represent the relaxation curve, but there are more options for creating the loading curve. A fixture of a QLV model is that combining the two parts using convolution, and this means that the two curves will have an effect on one another. The prony series is ultimately describing more than just the relaxation behavior, and whatever

equation is selected for the loading behavior will similarly affect the relaxation. It has been demonstrated by Troyer and Puttlitz that cervical spine ligament stress responses are strongly dependent on strain magnitude, indicating that a QLV model is not an effective model for some biological purposes [79].

Viscoelastic Convolution Model (LS-DYNA Model)

This is a specific case of the QLV model. This model generates a stress response containing both information about the elastic response and information about the viscous time-dependent behavior. Functions describing each portion are then combined using a convolution integral. The convolution integral contains a convolution kernel, $k(x - t)$ or $k(t - \tau)$. The integral also generally contains a partial differential term that describes the elastic stress. Each of these material model implementations contains a convolution integral representation of the stress that introduces the viscoelastic behavior. In each case, the user defines the viscoelastic response through a prony series, a sum of exponential terms. The prony series captures the relaxation response of the material being modeled.

3.2. Available DYNA Material Models

MAT 092

This material model is a hyperelastic model for simulating biological materials with transverse isotropy. The material model has been applied for use in representing ligaments in a model of a lower leg [80]. A hyperelastic strain energy function is used to define the stress in each element. This strain energy function is composed of two isotropic matrix terms, a fiber term, and a bulk term. The strain energy function is as follows (all following equations are from the LS-DYNA Keyword User's Manual vol. II [81]):

$$W = C_1 \left(\tilde{I}_1 - 3 \right) + C_2 \left(\tilde{I}_2 - 3 \right) + F(\lambda) + \frac{1}{2} K \left[\ln(J) \right]^2$$

In this model, the terms \tilde{I}_1 and \tilde{I}_2 are the deviatoric invariants of the right Cauchy-Green deformation tensor. C_1 and C_2 are the Mooney-Rivlin coefficients associated with the matrix surrounding the collagen. $J = \det(F)$ is a term that represents the volume ratio of the material.

λ is the deviatoric part of stretch along the fiber axis. $F(\lambda)$ is a function that describes the stress response of the embedded fibers, representing collagen bundles. Its derivatives are designed to model the uncrimping behavior of collagen during mechanical loading. They are given by the following piecewise function:

$$\frac{\partial F}{\partial \lambda} = \left\{ \begin{array}{ll} 0 & \lambda < 1 \\ \frac{C_3}{\lambda} \left[\exp(C_4(\lambda - 1)) - 1 \right] & 1 < \lambda < \lambda^* \\ \frac{1}{\lambda} (C_5 \lambda + C_6) & \lambda \geq \lambda^* \end{array} \right\}$$

In this function, the critical stretch ratio, marked as λ^* , is considered to be the point where the fibers are un-crimped. For $\lambda < \lambda^*$, the toe region of the curve is described as an exponential function, controlled by the constants C_3 and C_4 . For $\lambda \geq \lambda^*$, a linear function describes the curve. In this model, C_5 is chosen by the user, and C_6 is chosen by the computer to preserve continuity at the value λ^* .

Viscoelasticity is included using a convolution model representation of the second Piola-Kirchoff Stress. S^e represents “the elastic part of the second PK stress as derived from the strain energy”. $G(t-s)$ is the reduced relaxation function. In this model, it is represented by the Prony series below.

$$\mathbf{S}(\mathbf{C}, t) = \mathbf{S}^e(\mathbf{C}) + \int_0^t 2G(t-s) \frac{\partial W}{\partial \mathbf{C}(s)} ds$$

Relaxation Function Prony series

$$G(t) = \sum_{i=1}^6 S_i \exp\left(-\frac{t}{T_i}\right)$$

MAT 176

This material model is an isotropic formulation of the 1D QLV model proposed by YC Fung [36]. It is used to represent general soft tissues. There are 3 forms of this model, and they differ

in their representations of the elastic response, $T^{(e)}(\lambda)$. FORM = 0 is the original implementation of this material, and it incorporates the following equations for viscoelastic stress and relaxation:

$$\sigma_V(t) = \int_0^t G(t - \tau) \frac{\partial \sigma_\varepsilon[\varepsilon(\tau)]}{\partial \varepsilon} \frac{\partial \varepsilon}{\partial \tau} d\tau$$

$$G(t) = \sum_{i=1}^n G_i e^{-\beta t}$$

The relaxation function is modeled here as a prony series. The form uses the following series to approximate the elastic response:

$$\sigma_\varepsilon(\varepsilon) = \sum_{i=1}^k C_i \varepsilon^i$$

It is noted that by using only odd powers of ε , the generated $\sigma_\varepsilon(\varepsilon)$ response will be symmetric in tension and compression. This form will relax to zero stress as the time approaches infinity.

FORM = 1 uses a hyperelastic model elsewhere applied for rubber. The 1D expression for σ_ε is used to generate the stress-strain curve, and a viscoelastic term is added, σ_V . The following figure depicts this expression.

$$\sigma(\varepsilon, t) = \sigma_{SR}(\varepsilon) + \sigma_V(t)$$

$$\sigma_V(t) = \int_0^t G(t - \tau) \frac{\partial \varepsilon}{\partial \tau} d\tau$$

This form of the elastic response has the benefit of relaxing to a non-zero value, specifically the hyperelastic stress, σ_{SR} . The final formulation of this model is FORM = -1, where the elastic response is used to update the viscoelastic stress σ_V . This means that the constants of the elastic response will not need to be scaled.

MAT 266

This material model is an invariant formulation for soft tissues having dispersed orthotropy, for example a heart valve. The stress response of this material model consists of a neo-hookean

isotropic part, an active anisotropic part that is used to represent muscle contraction, and a passive anisotropic part that represents one or two families of collagen fibers, which are modelled either using a simple exponential model or a more complex crimped-fiber model, depending on the application. The expression for the second Piola-Kirchoff Stress (PK2) is given below. When modeling soft tissue such as sclera, the active part representing a contractile force is not used.

$$\mathbf{S} = \kappa J(J - 1)\mathbf{C}^{-1} + \mu J^{-2/3} \mathbf{DEV} \left[\frac{1}{4} (\mathbf{I} - \bar{\mathbf{C}}^{-2}) \right] + J^{-2/3} \sum_{i=1}^n [\sigma_i(\lambda_i) + \varepsilon_i(\lambda_i)] \mathbf{DEV}[\mathbf{K}_i]$$

In this equation, \mathbf{S} is the PK2 stress tensor. κ is the bulk modulus, μ is the isotropic shear modulus σ_i is the passive fiber model used, and ε_i is the active fiber model (not used here). J is the Jacobian of the deformation gradient, \mathbf{C} is the right Cauchy-Green deformation tensor, and \mathbf{DEV} is the deviatoric projection, given below.

$$\mathbf{DEV}[\bullet] = (\bullet) - \frac{1}{3} \text{tr}[(\bullet)\mathbf{C}]\mathbf{C}^{-1}$$

In this case, the variable λ represents the stretch ratio of the material, but since this model embeds the concept of dispersed fibers, it is more complex than simply the stretch ratio. λ is referred to in documentation as the dispersed fourth invariant. It is given by the following equation:

$$\lambda = \sqrt{\text{tr}[\mathbf{K}\bar{\mathbf{C}}]}$$

In this equation, \mathbf{K} is the anisotropy tensor or dispersion tensor, and $\bar{\mathbf{C}}$ is the isochoric portion of the right Cauchy-Green deformation tensor. The fiber model(s) used are effectively 1D models, and the tensor \mathbf{K} weights and rotates these models into the global Cartesian reference frame. The material model used for all following FE simulations was MAT 176, the Quasi-Linear Viscoelastic or QLV model. The QLV material model has two things that the other candidates do not. First, it can simulate time-dependent behavior, which is a failing of MAT 266, and second, it is isotropic, which is more appropriate than the transverse isotropy of MAT 092. Because the directions of anisotropy in the sclera of the whole globe are not completely known, the non-fiber

directions of the MAT 092 formulation would return stresses inconsistent with those in many regions of the globe, and so it was decided that a fully isotropic formulation was the better option.

Chapter 4: Mechanical Testing of Soft Tissues

With the recognition of the viscoelastic, hyperelastic, non-linear, and potentially anisotropic properties of soft tissues, it is necessary to consider the manner in which soft tissue samples can be obtained and tested to evaluate material properties. Careful consideration of the soft tissue will aid the test selection. Generally, there are two larger groups of material tests that can be performed, *in* or *ex vivo*. *In vivo* testing has been performed on various tissues with quality results. Non-invasive *in vivo* tests have been performed for human tissues on the femur [82], and more invasive experiments have also been successfully performed, for example on ACL tissue [83]. Most *in vivo* testing related to IOP in human eyes is performed during surgery [84, 85], although in one study human eyes were perfused with a radioactive tracer *in vivo* and then later enucleated for inspection of outflow pathways [86]. *In vivo* animal models are also commonly used when studying the eye, with notable examples of rabbit [87], rat [88], and monkey [89] models investigating different chemical modifications to outflow facility and IOP. For this work, we did not consider *in vivo* testing due to cost and regulation complexity. Instead, consideration was given to *ex vivo* testing methods. Within *ex vivo* testing, there are two general testing categories. Efforts can be made to duplicate the loading of the entire body (such as an eye or a ligament), or samples can be excised from the tissue for more conventional material testing.

Whole tissue testing

Often it can make sense to test whole ligaments, bones, or organs to attempt to understand the response of the entire tissue structure to imposed loading. Knee ligaments have been evaluated on cadaver limbs with partial dissection of the surrounding knee capsule and directional force application through the ACL [90]. In the case of eye globes, inflation tests are routinely performed by removing, fixing or altering some of the globe and mounting it to an inflation testing apparatus. The globe is then manually inflated and measurements are taken. Fixing the globe with a needle bisecting the center has been used to study scleral creep [91] and to compare inflation and uniaxial testing [63]. Another method separates the posterior scleral shell from the

anterior chamber, clamps and inflates the spheroid using PBS. This method allows for clear association of displacements with globe pressure, and has been used successfully to correlate measured displacements with FE model results [92, 93]. Another general method for fixing and measuring the globe involves using adhesive around the central region and then imaging a region of the globe to gain insight into pressure-strain relationships [94, 95].

Testing of the whole tissue can also be performed without fixing. Simply perfusing the globe with fluid, causing it to inflate, and characterizing the response using various sensing equipment is a less invasive method for tissue characterization. Unfixed perfusions are a common way to test whole globes and various perfusion methods have been used to good success [96-100]. In this work, unfixed enucleated porcine globes were perfused to understand vein and tissue strains associated with IOP changes induced by steady infusion of isotonic saline.

Mechanical Testing of Excised Samples

This method allows for very repeatable tests to be performed on highly regular tissue samples. Material samples are often extracted as either circular biopsy samples for compression testing, or for tensile testing as rectangular strips or less commonly dog-bone shaped samples. Biaxial material testing can also be performed on square tissue samples. Unconfined compression tests of biopsy samples have been used to inform a biphasic material model of sclera [101] and to study the effects of age on tissue properties during stress relaxation testing [102]. Tensile testing has been performed extensively on corneal and scleral strips [63, 103-107]. Tensile testing can also be performed using tensile dogbone specimens, an approach demonstrated on rabbit [108], monkey [109], bovine [68], porcine [99], and human [110] eye tissue samples. Dogbone-shaped samples are effective in concentrating the uniaxial loading of the sample within the gage length, but they can be more challenging to produce and often require a specialized punch. Biaxial mechanical testing can offer better perspective into the anisotropic variations of sclera tissue. Such testing has been used to identify differences in strains in circumferential and meridional directions [111], and to describe the anisotropic ratio of those directional tissue displacements [112]. For the purposes of this work, uniaxial testing was more accessible due to the lack of specialized equipment to perform many biaxial mechanical tests. Of the remaining options, it was chosen to study uniaxial tensile tests on dogbone samples of material. Uniaxial tensile

testing allows for the direction of loading to be within the plane of the tissue as opposed to through the thickness of the tissue, and this was seen as an advantage in understanding the stress response to loading of sclera.

4.1. Testing Procedures

4.1.1. Globe Perfusion Testing

The purpose of the present globe perfusions is to establish an imaging agent in the aqueous veins for the measurement of their strains by photoacoustic imaging[113]. The results of these experiments and analyses were recently reported in [100]. The globe preparation and perfusion procedures described next are extensions of procedures developed previously in [99], which did not involve an imaging agent.

Globe Preparation

Intact porcine eyes were obtained from two local slaughterhouses: Milligan's Northwest Meat Market, 7051 Standish Rd., Jackson, Michigan, USA, and Scholl Slaughterhouse, 1305 S. Piotter Hwy., Blissfield, Michigan, USA. Both have been inspected and approved by the United States Department of Agriculture, Food and Safety Inspection Services for humane handling of livestock. Eyes were kept in a closed cooler filled with ice with all fat attached.

Whole porcine eyes were sourced from two slaughterhouses: Milligan's Northwest Meat Market, 7051 Standish Rd., Jackson, Michigan, USA, and Scholl Slaughterhouse, 1305 S. Piotter Hwy., Blissfield, Michigan, USA. Both have been inspected and approved by the United States Department of Agriculture, Food and Safety Inspection Services for humane handling of livestock. The eyes were purchased with a layer of surrounding fat and connective tissue that maintains hydration. Once purchased, the eyes were stored in a contained maintained near 0C. Experiments were performed the morning after the animal was slaughtered to preserve the natural state of the eyes. Eye preparation followed procedures that had been described previously. The eyes were first trimmed of fat, muscle, and connective tissue, using medical scissors and forceps. Care was taken to not scrape or tear the scleral tissue. The fat capsule can be detached from the eye without much damage if the blades of the medical scissors are used to spread the tissue instead of cutting. The optic nerve was trimmed to be flush with the posterior

sclera. During dissection, the eye was periodically moistened with balanced salt solution (BSS). Once fully trimmed, the eye was placed into a large centrifuge tube containing a Kimwipe (Kimberly-Clark Professional, Irving, TX) moistened with BSS. Another Kimwipe moistened with BSS was placed on top, and the tube was stored on ice until it was time to perform the perfusion. When it was time, the tube containing an eye was placed into a water bath set to 37C. After approximately 15 minutes, the eye was removed from the water bath, and a laser thermometer was used to verify that the eye was at physiological temperature.

Perfusion Testing

While the eye was being warmed in the water bath, the experimental setup was also assembled. three lengths of tubing (Tygon ND-100-65, ADF0004, 5/32 inch outer, 3/32 inch inner, Saint-Gobain North America, Malvern, PA), were cut. The lengths were approx. 6", 8", and 14", respectively. A pressure sensor (Argon DTXPlus Model DT-XX, Argon Critical Care Systems Singapore Pte. Ltd, Singapore), two 21 gauge needles, and two 10cc syringes were also used. The perfusion experiment was found to function best when two lines of tubing were prepared. The first line was assembled as follows: One syringe was filled with BSS. It was connected at one end to the shortest length of tubing. BSS was pushed slowly into the tube, taking care to monitor for any bubbles in the fluid. Once the line was full of BSS, it was carefully connected to the bottom of the pressure sensor, and BSS was pushed through so as to fill the entire pressure sensor. When the pressure sensor was filled, the 8" length of tubing was connected to the top of the sensor, and it too was slowly filled with BSS. A 21 gauge needle was attached to the far end of the 8" segment of tubing, and then a stopcock on the sensor was turned so that fluid would not flow back out of the system. The second line of tubing was for imaging agent (ICG), so the second BD syringe was prepared with approx. 7cc's of ICG. It was attached to the 14" length of tubing and the tubing was filled as above. Once full, the second 21 gauge needle was attached to the ICG tubing.

The eye was then taken to the experiment room. An eye holder mounted on an articulating platform and stand was placed into position under the laser imaging setup. The holder included a custom water jacket that circulated water at 37C, helping to maintain the condition of the eye. A Kimwipe moistened with BSS was placed into the eye holder cavity. The eye was then

positioned in the cavity, with the cornea facing up. The holder was moved so that the eye was directly under the imaging system, and the focus of the system was adjusted. Once the focus was set, the eye was moved out from under the imaging system to prepare the perfusion setup. The BSS line was the connected first. The pressure sensor was mounted with tape on a metal pole so that its sensor was at the same height as the eye in its holder. It was important that the lengths of tubing permitted the pressure sensor to be mounted nearby while the needle could still easily reach the eye. The pressure sensor was connected to the computer system. BSS was pushed into the needle until several drops came out to verify that there was no air in the end of the line. The length of the needle was then held against the surface of the eye, near to its anticipated configuration in the eye, and the pressure reading was zeroed in the computer system. Once the pressure reading was stable around 0 mmHg, the needle was inserted through the cornea, through the anterior chamber (AC), and positioned so that its tip rested in the posterior chamber. Care was taken to avoid clipping the other bodies in the anterior chamber (iris, lens) with the needle tip, as that could cause the needle to become blocked. With the needle in the eye, a note was made in the pressure monitor program of the eye's initial pressure. Next, the ICG needle was inserted into the AC. The needle was inserted so that it sat in the AC, above the iris. With both needles in the eye, the eye holder stand was carefully moved back into position under the imaging system. A cover was placed over the eye in its holder to help maintain temperature and humidity.

The eye was then pre-conditioned according to a defined protocol [99]. First, the IOP as read from the pressure software was raised to 15 mmHg over the course of 2 minutes. Then, the pressure was maintained at 15 mmHg for another 2 minutes. Finally, the eye was allowed to relax with no external fluid pressure for 3 minutes. After 3 cycles of this pre-condition, the eye was deemed ready to test. At this point, the ICG syringe was placed into a syringe pump, and the pump was set between 6-9 $\mu\text{L}/\text{min}$. As ICG flowed into the anterior chamber, the pressure was monitored and the eye was periodically checked for visible staining of outflow networks. Once several veins were visibly filled with dye, the pressure was adjusted so that it was within a range of 20-28 mmHg, and images of the veins were taken. The pressure was then lowered by 2 mmHg

increments, with pictures being taken at each step down in pressure. When the eye had reached its initial pressure value recorded earlier, the experiment was finished.

4.1.2. Sample Mechanical Testing

When mechanical testing was to be performed on porcine eyes, there were several potential procedures to be followed. Above all else, the main goal of performing mechanical tests was to collect tensile data that could be used to create and inform models of sclera tissue behavior, with the intention of using this tensile data to better understand the sclera's response to perfusion. From the beginning, both tensile and compressive tests were considered. Tensile tests were ultimately chosen as the preferred data collection method. It was perceived that tensile data of the porcine sclera samples would be effective in describing the in-plane stresses experienced by the whole globe during perfusion tests. To conduct tensile tests, there are two further options. The tensile test can either be conducted to failure of the tensile dogbone sample, or it can be conducted to some prescribed stress value. If the test is performed to a prescribed stress value, the sample can subsequently be held at a constant elongation, and data can be collected about the stress relaxation behavior of the tissue.

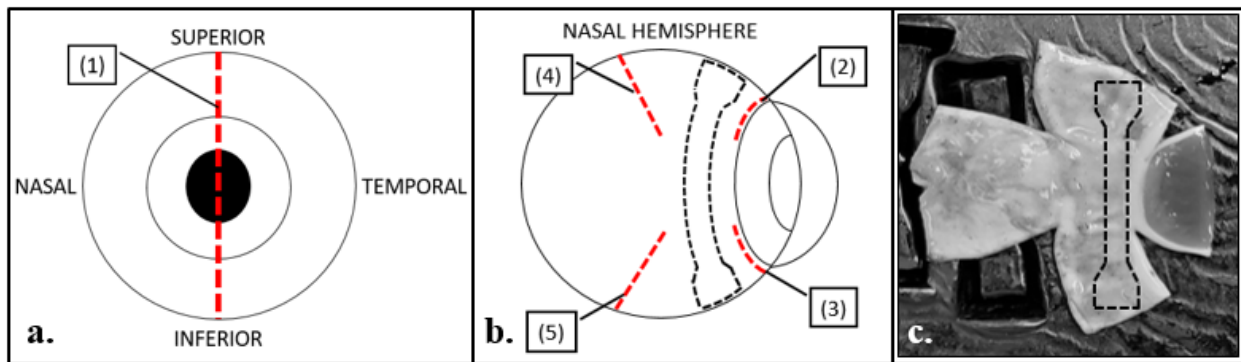


Figure 3: a. depicts the first cut splitting the two hemispheres of the globe, b. shows the ensuing cuts to flatten the hemisphere, c. depicts the approximate location for the excised dogbone on the flattened tissue region.

Eye Preparation for Mechanical Testing

A solid metal dogbone cutting die produced by TestResources was used to remove the dogbone samples from the globe. First, the globe was removed from its specimen tube and the tube was returned to the refrigerator. The area of tissue to be stamped was dried with a medical swab. The cutting surface of the tool was marked with a Devon skin marker, and then it was pressed gently against the surface of the globe. This left a clear marking of the tissue region that would be

punched out with the cutting die. A diagram of the globe is given above in Figure 3 to better explain the nature of the dissection. The globe was then split into 2 hemispheres by cutting circumferentially along line (1), Figure 3 a. Each hemisphere was placed into a weighboat and covered with BSS temporarily to protect the tissue. Next, one of the hemispheres was taken and prepared to be stamped with the cutting die. The interior surface of the hemisphere was trimmed of the iris and retina structures so that they would not interfere in testing. The iris was gently grasped using forceps and then it was pulled away from the corneoscleral junction, an action which requires only a small amount of force. This action would also often bring the retinal tissue layer along with it, but when it did not, the retina was grasped using forceps in much the same manner and gently pulled away from the interior surface of the sclera. It was only necessary to remove the retina tissue from the anterior portion of the hemisphere, as the dogbone samples were only excised from the perilimbal sclera tissue. The retina was noted to be anchored to the interior surface of the eye b only a few points, and so by carefully removing the retina at one of these points, a large region of retina would fall away from the sclera with little force applied. After this preparation, the hemisphere was placed with its interior surface facing down, and four cuts were made according to Figure 3 b. Cuts (2) and (3) were made to detach the perilimbal region from the cornea, and cuts (4) and (5) were made to flatten the tissue so that a sample could be punched. The outline of the dogbone sample is also seen in Figure 3 b. to show how the sample follows the globe's curvature. After the cuts (2)-(5) were made, the hemisphere was gently spread out flat on a wax cutting tray, pictured with the approximate outline of an excised dogbone in Figure 3 c. From this position, the cutting die was placed over the perilimbal region and was driven through the tissue using a few swift strikes from a corked mallet. The excised dogbone sample was then gently removed from the tray and placed into a labeled weighboat with BSS. The cutting and sample stamping process was then repeated on the opposite hemisphere, and the two samples were taken to be measured before mechanical testing. The samples were measured for their tissue thickness at three points along the gauge length of the dogbone, and those numbers were averaged to provide an estimate of the dogbone sample thickness. The width of the sample and its gage length were both treated as constant values due to the shape of the dogbone cutter. The width was very rarely noted to be different from that of the sample cutting

die, and in those cases the width was also measured and recorded in the same manner as the thickness. After measuring the samples and recording those values, the paired samples were placed into the temperature and humidity controlled chamber surrounding the uniaxial testing grips to allow them to reach physiological temperature.

Tissue Stiffening Protocol

The artificial stiffening of soft tissue is a useful and necessary pursuit for many different areas of research and clinical practice. In the case of porcine sclera tissue stiffening, two main stiffening protocols were tested. The first protocol was designed using riboflavin and UV light to

First a 0.5% genipin solution is created from 5mg genipin powder dissolved in 1 mL BSS. It was noted that 30 mg powder and 6 mL BSS created enough genipin solution to treat 4 eyes. This permits for 4 pairs of eyes to be prepared and then tested for a discernible stiffening effect. A spongy tissue (PILLING Weck-sorb weck-wipes, Teleflex, Wayne, PA) was trimmed into a half-annulus shape, with inner diameter (ID) approx. 12mm and outer diameter (OD) approx. 18mm. 2 or 3 half-annulus pieces of Weck-sorb were used to completely cover the limbus region of each eye, depending on its size. Pairs of porcine globes that had been trimmed of their fat and connective tissue (as described above) were prepared and then placed in specimen tubes with BSS-moistened Kimwipe on ice. Meanwhile, half of the Weck-sorb half-annulus pieces were placed into a weigh boat and covered with the 0.5% genipin/BSS solution until the solution covered all the sponge pieces. The other half of the prepared half-annulus pieces were placed into a weigh boat and covered similarly with BSS only. Next, the porcine globes were removed from their specimen tubes and patted dry with tissue. The globes were placed, with the pupils pointed vertically up, inside of the specimen tube caps. They were surrounded by a BSS-moistened tissue to prevent desiccation of the globes during the treatment. The eye of each pair to be treated with genipin solution was chosen randomly by flipping a coin. The genipin-treatment eyes were aligned in a row, with the corresponding control eyes of each pair forming a parallel row behind them. The moistened genipin and control half-annulus sponges were placed onto the globes, covering the limbus region of each one. After all limbal regions were covered with a sponge, a timer was started, and 6 drops of either BSS or 0.5% genipin/BSS solution were administered onto the sponges on each globe every 5 minutes. The drops were administered from

a 20G needle to maintain a consistent droplet size. After 30 minutes had elapsed, the globes were treated topically with the solutions one final time, washed with BSS, and placed back into specimen tubes with moistened tissues. The tubes were organized and placed into a 4C fridge for 24 hours to await tensile elongation (TE) and stress relaxation (SR) testing.

Tensile Testing Apparatus

The tensile tests were performed using a TestResources (TR) machine (TestResources 225lb Actuator, Shakopee, MN) configured to actuate horizontally. The TR machine was modified to include a Plexiglas chamber and lid that surround the area of the grips. During testing, a heating coil was placed into a dish containing BSS and used to raise the temperature within the chamber to 37°C during tensile testing. A Thermo Hygrometer was used to monitor the temperature and relative humidity (RH) in the chamber during tensile tests. An attached TR Box was used to set the testing mode and control the tests. The data log rate could be adjusted, which indirectly determined the maximum test length. After testing, the data of each individual run was exported from the TR Box via a USB drive or a USB cable connection to a computer as a comma-separated value (CSV) file. The data is then processed further using Microsoft Excel.

Tensile Elongation Testing

To perform a TE test, the controller was set to run at the prescribed strain rate to an arbitrarily long extension (60 mm). As the TE test advanced, the dogbone sample was visibly stretched and then it would begin to pull apart. This pulling apart was accompanied by a dropping of the measured force within the sample, as is visible in the following stress-strain graph. As the measured stress dropped back to a near-zero stress state with increasing elongation, the test would be stopped. In the displayed case, the stress was allowed to drop to zero before the test was completed.

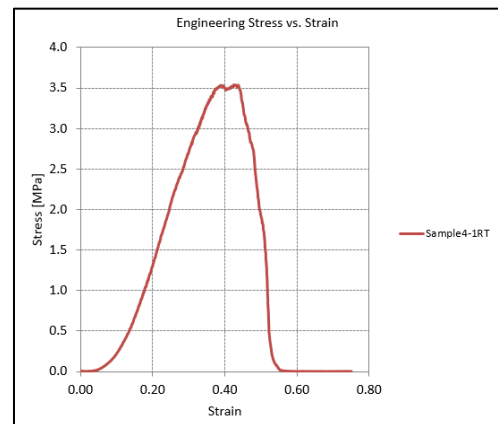


Figure 4: tensile elongation test data showing stress level through failure of sample

Stress Relaxation Testing

To perform a SR test, the controller was programmed with two test segments. The first test segment was similar to the TE test segment, where the controller was set to run at a prescribed strain rate. Instead of the termination flag being an arbitrarily long extension, a prescribed stress level was established (0.14 MPa) and the test segment was set to end upon reaching this stress level. To input this prescribed stress, a prescribed force was calculated based on the measured cross-sectional area of each sample's gage length, and this force value was entered into the controller as the end point for segment one. Test segment two was simply set to a "strain rate" of 0 mm/min for a certain length of time, resulting in the tensile grips holding the sample steady at the elongation reached by test segment one. This test segment collected data on the stress relaxation behavior of the sample. It is noted by YC Fung in his text "Biomechanics: Mechanical Properties of Living Tissues" that ending a relaxation test prematurely causes the relaxation spectrum to appear complete, when it can indeed last much longer [36]. However, the relaxation spectrum of viscoelastic tissues can span well over 1000 minutes, and performing many SR tests with this amount of relaxation would simply not be feasible. Further, the simulation of these SR tests takes a longer time when the relaxation segment of the test is longer. Due to this reality, the relaxation segments of the SR tests were limited to 5 minutes. This was seen as a good compromise between the real-world time constraints of testing samples, and the necessity of collecting as much of the tissue relaxation spectrum as was possible.

4.2. Data Processing

Many tensile specimens would be tested on any given day of collecting tensile data. Therefore, the data would have to be processed to limit noisy data and single-test deviations from the standard behavior. Common deviations with the collected data included the aforementioned noisy data output, force readings starting at a nonzero value, a long toe caused by excessive slack in the sample, and slipping or premature tearing of samples leading to poor stress curves. Excessive noise in the data can be caused by vibrations in the same room as the tensile tests, or by collecting too much data each second. A nonzero force reading at time zero can be caused by zeroing the force in the recorder too early, or by the presence of a miniscule preload within the tissue. There is nothing to be done about slipped samples, as it is impossible to gauge when

during the test the sample began to slip. However, samples with noisy data or force readings starting at nonzero values can be processed to significantly improve the results. There is a simple solution in each of these cases.

Zeroing Data Curves

In the case of nonzero force values at the very beginning of a test, it is appropriate to zero those force values by a value such that the value at time zero is approximately zero. It is best to not “over-zero” the values, which can result in some negative values of the data curve. Simply subtracting the minimum value of the force within the first 5-10 seconds allows for the data curve to be sufficiently zeroed, without creating any negative values.

Smoothing Data Curves

When programming a material test into the TR Machine, the amount of data collected per second is tied to the length of the test segment. To perform a test that had total runtime of 5 minutes, the

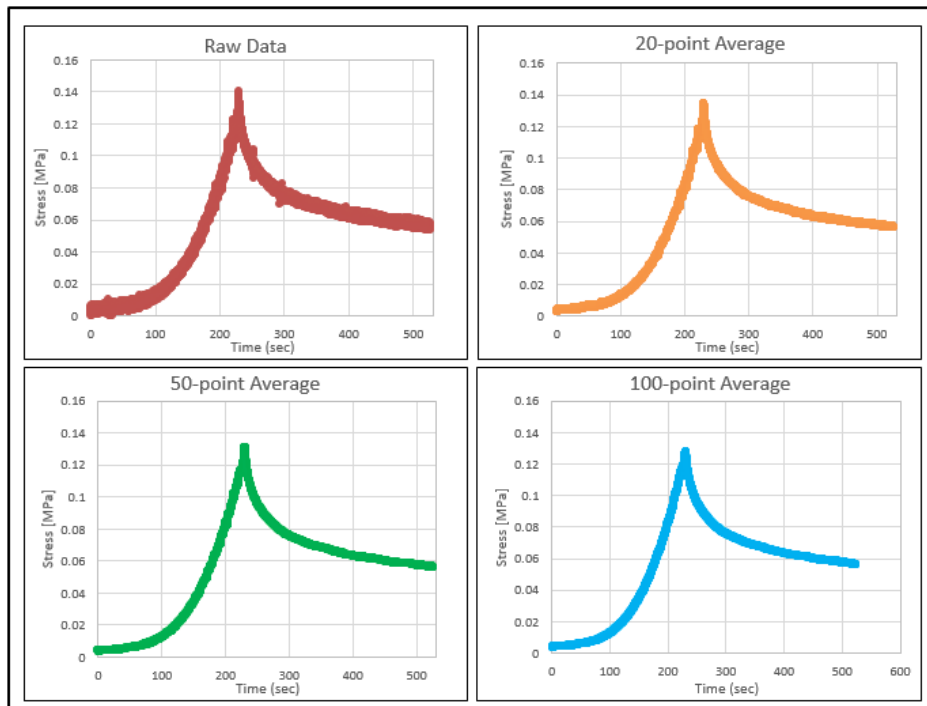


Figure 5: A sample raw data curve is shown along with 20-, 50-, and 100-point averages, highlighting the smoothing effect and lowering of the peak value induced by this process.

data would be sampled 25 times per second. This certainly captures the character of the data curve, but it leads to some excessive variance within the data. To combat this effect, several

moving averages were taken and inspected to determine the most appropriate amount of data to average. 10, 50, and 100 point moving averages were taken of a representative data curve, and they are depicted in Figure 5 along with the un-averaged data. Of these options, it can be seen that the choppy unaltered data becomes progressively smoother with increased averages. It is also clear that the peak stress reading is gradually lowered by the act of averaging the data. With these facts in mind, the 50 point average was chosen to smooth the data further than the 10 point average, while retaining more of the peak stress value than the 100 point average.

Trimming Data Curves

It is simply impossible to load each specimen from a zero-stress state. Further, it is not possible to mount each sample into the tensile grips in such a way that there will be no slack in any one of them, especially without applying a preload. As a preload was seen as more disadvantageous than slack in the tensile sclera

specimen, the samples were generally loaded in such a way that they sagged very slightly in the gage length region between the grips.

This naturally results in a small amount of slack in each tested sample. To remove this slack from each curve, the tangent modulus was plotted against the engineering stress. The tangent modulus is

calculated as the difference in stress at two points in time divided by the

difference of strain over that period. When different distances between the two points are chosen and plotted together, a set of curves showing the chaotic variance in tangent modulus during the slack portion of the data appears. This set of curves is shown in Figure 6. There is still some nuance in choosing the best point to trim the data, but plotting the tangent modulus against the stress at low stress values demonstrates a good starting point for the coherent data. In the Figure

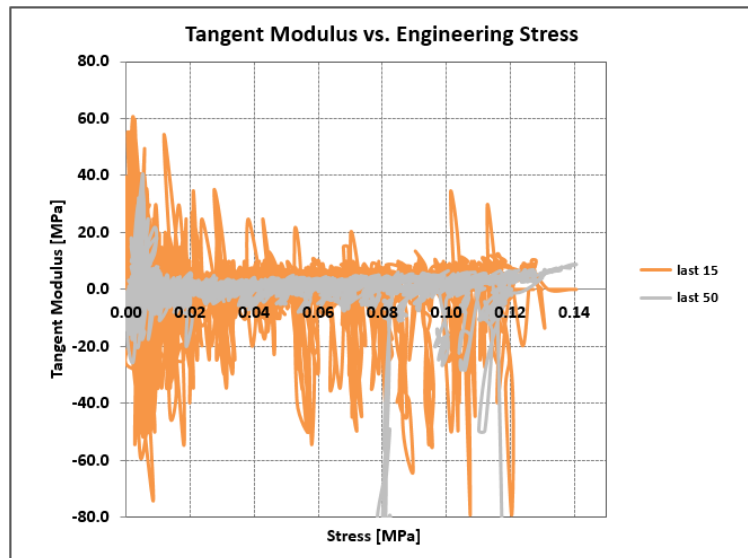


Figure 6: Showing the toe region based on the rolling Tangent Modulus vs. Stress calculation. This method predicts the end of the toe of this sample around 0.02 MPa.

6 case, the chart reveals that trimming the data at around 0.02 MPa will remove most of the slack from the curve.

To trim the data, all of the stress values before approx. 0.02 MPa are removed, and the rest of the data is shifted back in time accordingly. This process often results in non-zero stress values at time zero, and so the procedure described in “Zeroing Data Curves” to remap the data will also be performed.

Separation of Loading and Relaxation curves

After sets of stress relaxation data were collected, it was necessary to treat only the relaxation spectrum so that the 5 and 7 parameter viscoelastic solid material models could be fit to that range of data. At the same time, it was important to extract properties from the Stress-Strain portion of these curves, and so steps were taken to separate the two sections of data from the whole. Microsoft Excel sheets were created to this effect.

Treatment of Loading Data

To work with the Stress-Strain data, an Excel sheet was created that collected the strain and stress data output (as force and displacement measurements) from the uniaxial testing machine. MAX and MATCH functions were used to identify the peak stress value and return its row cell location. This was then used to jump to that row and delete all data below that row. A series of charts preloaded with the data ranges to be occupied were used, and the first of these showed the original Stress-Strain curve. This curve was then visually inspected, along with the Tangent Modulus vs. Stress curve, and a decision was made as to where the data would be trimmed. The stress and strain data columns were taken from that point down and copied to an adjacent location that then zeroed each column by slightly different means. As the strain data was constantly increasing, it could always be zeroed by its first value. The stress value was instead zeroed by its smallest non-negative value in the first 25 points. All negatives were removed from the curve in this region to prevent accidental shifting of the curve in the wrong direction. Next, a new L_0 value corresponding to the amount of elongation at the beginning of the trimmed data was extracted and used to re-calculate the strains. The trimmed SS data, the SS data using the new strain and a second set of the SS new strain data were all automatically filled into charts.

The second copy of SS new strain data was trimmed to only include the linear region of the SS data, and that linear region was fit by a first order polynomial to provide a tangent modulus.

Treatment of Relaxation Data

The MAX function was again used to identify the peak stress. Next, ADDRESS and MATCH functions were used to return the cell location of the peak stress in the original sheet. A CELL("row", INDIRECT()) function was then used to extract the row value of the location of the peak stress. This number was then additively iterated in a column for the length of the relaxation data, equal to either 300 or 600 seconds at however many data points/second were collected. This column's values were then used to create a column of cell addresses located under the address of the peak stress. Finally, the INDIRECT function was used to point to this column of addresses and return the stress values at each of those addresses, collecting all of the stress values after the peak stress and describing only the relaxation portion of the data in terms of time and stress. This relaxation spectrum was then normalized by creating a column that divided each stress value by the input strain to create the data set that was then used to calculate the 5-parameter and 7-parameter viscoelastic solid model parameters. A summary of the Excel functions used for these purposes is provided in Appendix 1.

4.3. Mechanical Testing Results

Results for the tangent modulus and stress at 8% strain are summarized in Table 1. It was found that the tangent modulus of the genipin-treated samples was significantly greater than the tangent modulus of untreated samples for both 0.5 mm/min ($p=2.92E-4$) and 10 mm/min ($p=6.78E-5$) test speeds. There was no significant difference between the tangent moduli for the 2 sets at 100 mm/min. The stress at 8% strain was found to be significantly higher for the 0.5 mm/min genipin-treated test case than for the untreated controls ($p=8.82E-4$), but this effect did not occur in either the 10 mm/min ($p=0.082$) or 100 mm/min ($p=0.599$) cases. The difference between genipin and control SR curve stress values at 10, 150, and 275 seconds was found to be significant for both strain rates.

Table 1. Stress at 8% strain and Tangent Modulus from Linear Region (mean \pm SE)

Rate (mm/min)	Treatment	Stress (kPa)	Modulus (MPa)
0.5	None	196.59 \pm 24.62	11.88 \pm 0.61
	Genipin 0.5%	329.06 \pm 44.23 (p = 8.82E-4)	15.62 \pm 1.05 (p = 2.93E-4)
10	None	330.95 \pm 33.36	12.5 \pm 1.25
	Genipin 0.5%	401.62 \pm 41.40	17.58 \pm 1.24 (p = 6.78E-5)
100	None	484.48 \pm 29.81	17.63 \pm 0.97
	Genipin 0.5%	513.53 \pm 55.49	19.32 \pm 1.16

The average values of the 5 and 7 parameter model coefficients are summarized in Table 2. The mean standard error of regression from the 5 parameter fits of the 100 mm/min data was found to be 68% greater than the same measure for the 7 parameter fits of that data. This indicates that the 7 parameter model is fitting the 100 mm/min data more completely than the 5 parameter model.

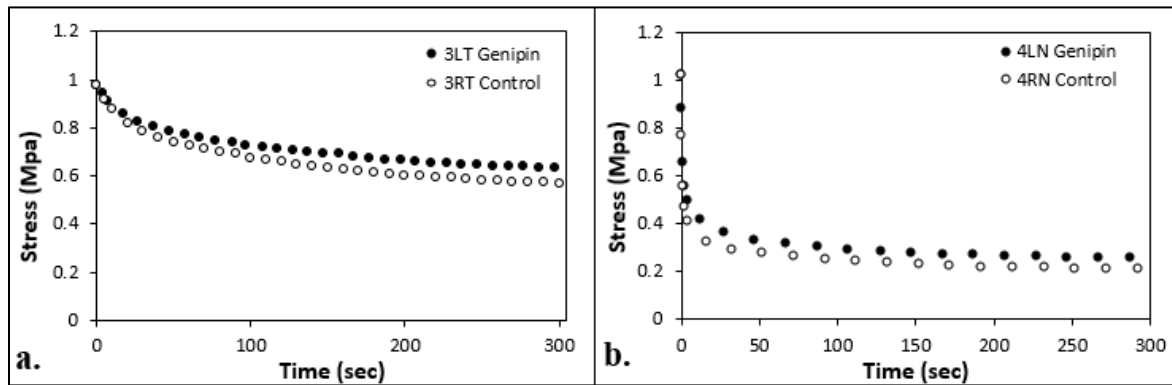


Figure 7: Representative 0.5 mm/min (a.) and 100 mm/min (b.) stress-time relaxation curves. The lower rate samples relax much less per unit time than the higher rate samples over the same time period.

Typical stress relax curves are shown in Figure 7a and 7b for 0.5 mm/min and 100 mm/min rate, respectively. The stress – log time charts of the stress relaxation data for each strain rate (Figures 8a-b.) determine the number of distinct slopes that would correlate to different relaxation rates and therefore different relaxation terms [114]. In Figure 8b for the 0.5 mm/min input stress relaxation case, 2 distinct linear regions are visible on the graph. This suggests that two distinct relaxation times would accurately fit the data and so a 5 parameter model, which corresponds to a three term Prony series, would sufficiently fit the data. Attempting to use a 7 parameter model for the low rate data produced highly correlated parameter results, where “highly correlated” in this case means that this model contains too many parameters to properly fit the data. The slope (modeled by the G_3 parameter) of the lower rate curve’s second linear region does not change when the 600 second relaxation period is used ($G_{3,300} = 2.29$ MPa, $G_{3,600} = 2.28$ MPa). For 100 mm/min SR curves, the S value for 7 parameter fits was 68% lower than the S value for 5 parameter fits, and the difference was statistically significant ($p < 1E-15$).

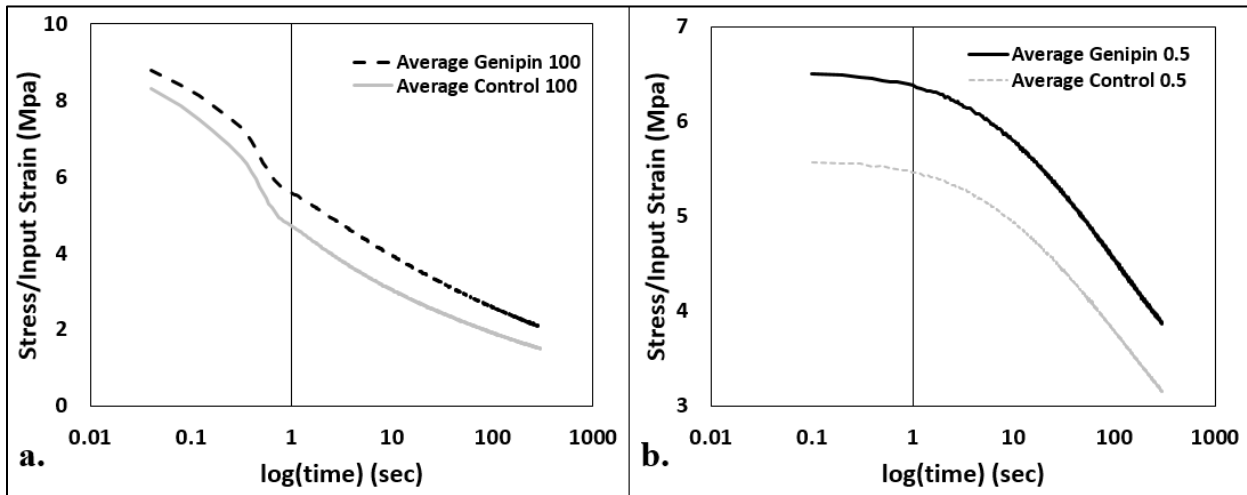


Figure 8: Stress-log(time) charts of the average high and low rate sample data. Note that the low rate data Y axis is truncated to better highlight the curve shape.

Table 2. 5 Parameter and 7 parameter model coefficients (mean \pm SE)

	0.5 mm/min		100 mm/min			
	5 Parameter model		5 Parameter model		7 Parameter model	
	Untreated	Genipin 0.5%	Untreated	Genipin 0.5%	Untreated	Genipin 0.5%
G1 (MPa)	2.98 \pm 0.19 (p = 6.56E-5)	3.71 \pm 0.22	1.56 \pm 0.11 (p = 0.005)	2.12 \pm 0.14	1.47 \pm 0.10 (p = 0.005)	2.00 \pm 0.13
G2 (MPa)	0.87 \pm 0.09	0.94 \pm 0.08	3.82 \pm 0.17 (p = 0.016)	3.26 \pm 0.15	4.12 \pm 0.18	3.70 \pm 0.17
G3 (MPa)	1.73 \pm 0.15	1.86 \pm 0.16	1.56 \pm 0.10	1.81 \pm 0.13	1.64 \pm 0.09	1.73 \pm 0.12
G4 (MPa)					1.25 \pm 0.09 (p = 0.029)	1.50 \pm 0.12
τ2 (s)	14.54 \pm 0.51	14.54 \pm 0.80	1.78 \pm 0.12 (p = 0.003)	2.66 \pm 0.23	0.50 \pm 0.01 (p = 0.042)	0.534 \pm 0.01
τ3 (s)	146.21 \pm 5.27	140.6 \pm 5.93	64.35 \pm 1.97 (p = 0.022)	72.14 \pm 2.73	7.99 \pm 0.28 (p = 2.77E-4)	9.78 \pm 0.24
τ4 (s)					100.43 \pm 2.77	110.54 \pm 3.58
v2 (MPa·s)	12.9 \pm 1.48	14.06 \pm 1.76	6.78 \pm 0.53 (p = 0.014)	8.62 \pm 0.80	2.05 \pm 0.10	1.97 \pm 0.09
v3 (MPa·s)	256 \pm 26.13	264.49 \pm 28.98	101.88 \pm 8.19 (p = 0.006)	132.75 \pm 11.71	13.20 \pm 0.99 (p = 0.012)	16.92 \pm 1.25
v4 (MPa·s)					127.49 \pm 10.89 (p = 0.006)	165.83 \pm 13.69

4.3.1. Discussion

Porcine sclera has been used to evaluate tensile properties by many researchers, frequently to understand the mechanical properties in the context of the optic nerve head. A stress between 0.3-0.4 MPa was measured in posterior porcine sclera samples, and the digestion of sGAGs did not have a significant effect on the results [105]. The sclera has been tested in anterior, equatorial, and posterior regions, showing a clear variation in properties between those regions. An experiment with 64 total tensile sclera strips tested for elastic modulus and grouped by sample location, there were found to be significant differences in anterior and posterior sclera samples, and there was also found to be a significant correlation of sclera stiffness with age [115]. Another study of the relationship between birefringence of sclera and regional properties showed tangent modulus correlation in the equatorial region, and stiffness correlation in the

anterior and equatorial regions [116]. This demonstrates a regional tissue property variation that is only correlated with tissue properties not found in the posterior region of the eye. An experiment seeking to quantify the variation of regional property variance in human sclera found a trend of increasing stiffness when moving from posterior to anterior sclera, and also noted a significant difference in stress and modulus with an increased strain rate [103]. It was suggested that the variability of samples within each group is the reason that the progression of stress and modulus from posterior to anterior regions was not statistically significant. A general sample-to-sample variability was also apparent in our data set, and it is possible that this also obscured any potential statistical significance that were not observed. A more recent study seeking to discover regional property variation and the effect of preconditioning on human eye samples showed the same posterior to anterior stiffness increase, and found little effect of preconditioning on the coefficient of variation for any region except the peripapillary region and ONH [117]. Preconditioning was noted to have lowered the entire stress-strain curve and increased its tangent modulus.

In a study of strain-rate sensitivity of corneas, a strain rate of 0.8%/min (equivalent to 0.10 mm/min with 13mm gage length dogbone samples) was stated to be close to the strain rate within the eye during the process of moving from standing or seated positions to supine [118]. A strain rate of 420%/min (equivalent to 54.6 mm/min) was further stated to be between that of eye rubbing and non-contact tonometry [118]. The highest strain rate used in the present work, 100 mm/min, was chosen to highlight the viscoelastic relaxation behavior of the tissue, and this was based on previous research performed at that rate [99].

The use of uniaxial tensile data to draw conclusions about *in vivo* globe stress-strain behavior is complicated by the relatively different conditions of each type of tests. Wong et al. investigated the effect of crosslinking whole globes, using IOP as a stress analog and estimating strains from image tracking data. This study found that the stiffness of the toe region was significantly greater in some crosslinked groups than in their paired control globes [119]. Another work by some of the same group members seeking to relate the posterior sclera uniaxial tensile properties to properties acquired during whole-globe inflation testing found that uniaxial tests produced peak strains twice as high for the same stress as inflation tests, and that the inflation test data had

generally shorter toe regions, stiffer stress-strain curves, and overall reduced variance [63]. This group used the LaPlace pressure vessel model to estimate the circumferential tissue stresses in the globes, which raises some problems since it is for perfect spheres and so is overly idealistic. Though the LaPlace model is a reasonable approximation of any case that approaches the ideal state, soft tissues have much more complexity in their stress response, and that will never be predicted by such a model. These globe inflation results suggest that although uniaxial tensile testing can give some insight into the behavior of sclera *in vivo*, more work must be done to understand tissue properties in whole globes and under inflation loading conditions [63].

Sclera is known to be crosslinked naturally through the process of aging [14]. There are also many different chemical agents that can be used to artificially crosslink collagenous tissues, either through physical or chemical means [120]. The effects of collagen crosslinking on uniaxial tensile testing results have been well documented. A study using Riboflavin with UVA light, glyceraldehyde, and glutaraldehyde to crosslink separate groups of tensile samples demonstrated that all of these agents would significantly increase the stress at 8% strain in both human and porcine sclera [121]. It was also noted that the quadrupled stress at 8% strain from untreated porcine to untreated human sclera was statistically significant, demonstrating that there are some fundamental differences between human and porcine sclera tissue. Two more works studied the effect of genipin crosslinking agent in a rabbit model by excising tensile strips from treated and untreated paired eyes. The first used Riboflavin/UVA treatment on live rabbits, and extracted the samples after 3 days. This study evaluated the ultimate stress of the samples and found a 341% increase in tangent modulus from the untreated to treated sample set [122]. The other study also used live animal terminal study to evaluate a genipin crosslinking agent and found a 130% increase in stress at 10% strain from untreated to treated samples. Despite the difference of these two crosslinking processes, it is apparent that many different physical and chemical crosslinking agents can provide strong crosslinking effects [123]. Liu and Wang studied the effects of different concentrations of genipin solution and two different treatment times on the resultant stress-strain curves. They found that the stress at 8% strain was increased for all sets treated for 30 minutes and for some of the higher concentrations of genipin treated for 15 minutes. The same pattern of significance was found for Young's Modulus values measured at 8% strain

[124]. This data was collected at a strain rate of 1.5 mm/min, equivalent to about 2 mm/min for our gage length. The control data set of this study in particular showed good agreement with our 0.5 mm/min data, though our genipin data from that group shows less crosslink effect than their set does for any concentration of genipin treated for 30 minutes.

The significance of the 100 mm/min SR results was anticipated from the beginning of this project, as the input condition is the closer of the two tested SR conditions to the theoretical step-input ϵ_0 for which the stress relaxation test is defined. This condition is critical for generating complete relaxation spectra of collagenous tissues such as ligaments, tendons, or bone.

Crosslinked collagenous hydrogels have demonstrated a visible difference in relaxation curves between control and treated hydrogels [125]. Another study of bovine cornea demonstrated that crosslinking can increase the equilibrium stress and the peak stress for a particular strain with statistical significance [104]. Crawford Downs et al. investigated early glaucoma monkey eyes against non-glaucomatous eyes and showed that the equilibrium stress of the glaucomatous eyes was significantly greater than that of the normal set [126]. Our 5-parameter model results demonstrate this with the increased G_1 value for treated samples. The G_1 parameter is tied to the free spring in the parallel spring-damper model, and it determines the equilibrium stress value as the test time goes to infinity. This was the only significant value we found at the lower rate SR test, demonstrating that the increased long-term (equilibrium) stress value effect persists across the range of testing rates explored here. There was strong significance of both v_2 and v_3 at the 100 mm/min rate, showing that the parameters related to slower effects in the tissue stress response to high-rate inputs were increased by the genipin crosslinking procedure. The relaxation time constants (τ) are a result of the relationship $\tau_i = v_i/G_i$, and so their significance is seen as a consequence of other effects of the genipin crosslinking process. The time constants did increase for genipin samples, showing that genipin-treated tissues subjected to a high-rate process will relax slower than untreated tissues.

The significance of the SR curve Stress/Input Strain values at 10, 150, and 275 seconds demonstrates the effect of the crosslinking agent on the tissues across the complete relaxation period. This significance is reflected in the significance of the G_1 parameter across the 5 and 7 parameter models for both strain rates. There is no perceptible difference when adding 300

seconds' relaxation time at the 0.5 mm/min rate. It is possible that a more complex relaxation behavior could develop after 600 seconds of relaxation, but the amount of time required to perform a large amount of such relaxation tests would render the testing volume infeasible. The 100 mm/min data had a more complex shape in this representation with 3 distinct slopes, offering an explanation as to why adding a fourth Prony term improved upon the 5 parameter model fit.

Chapter 5: Optimization Using LS-OPT

In the present work, procedures were designed to optimize two different material models using LS-OPT. This solution was motivated by excellent simulation results generated in a similar study where a material model was optimized to simulate the behavior of a knee ligament [127]. Using the limited description from that study as a guide, optimization of the material model MAT_092, Soft Tissue (Visco) was undertaken to determine the material parameters that would best fit the collected tensile data. As the project progressed, it was determined that MAT_092 could not perform all of the desired modeling tasks sufficiently, and so a more appropriate material model was researched and implemented. The material model used for the remainder of modeling was MAT_176, Quasilinear Viscoelastic. There were many similarities in designing optimization routines for the two models, and each process will be described in detail.

The LS-OPT software package is available as a companion software package for LS-DYNA with which to explore a design space or to find optimal designs for specific input constraints. Though the software was made to interface with LS-DYNA, it can also be used with HyperMorph, Excel, MATLAB, or user-defined FE solvers. To design an LS-OPT experiment, a general task must be selected along with an according strategy. Some task options include metamodel or direct optimization, design of experiments (DOE) study design, or Monte Carlo simulation. A strategy is only chosen for metamodel-based optimization. Metamodel optimization is a tool that was developed as a substitute for complex simulations that are mathematically complex and very time intensive. By approximating those solutions using metamodels, the time and computation costs can be greatly decreased [128].

5.1. Consistent Settings

Parameterization of the K File

The PARAMETER card must be created for each LS-DYNA model to be run through LS-OPT. The PARAMETER keyword is presented as a series of paired entries, labeled “PRMRn” and “VALn”. A name for each parameter is entered in “PRMRn” and its corresponding value fills

“VALn”. To name each parameter, the first character must be R, I, C, indicating whether the parameter is a Real number, Integer, or Character. Following that character is a unique name, and it was found sufficient to use single alphabetical characters for parameter names, as “R a”, “R b”, “R c”, and so on. More descriptive names can be used of up to 9 characters. The “VALn” field is then filled with a starting value, which is less important when using this card to execute LS-OPT experiments. If the PARAMETER card were being used in another way, this value would be more critical. Next, the material model card must be edited to refer to the parameter names. This is best achieved by manually editing the keyword file in a text editing application, as it was noted that attempting to insert the references while in LS-PrePost would cause the program to crash. The parameter is referenced using an ampersand character (&) followed by the parameter name, e.g. “&a”. These references were inserted into the material card, and this caused the parameter values to be represented in the PARAMETER keyword when examining the file in LS-PrePost. The keyword file was then considered ready to use in LS-OPT, and was saved to the appropriate LS-OPT active folder. It is best if the active folder is located somewhere with sufficient disk space, such as the C: drive, as LS-OPT can generate many GB of data during a single optimization routine. The active folder should also be located within the same directory as the FE solver .exe file.

Overview of the OPT Routine

LS-OPT is fairly well documented, and simply running example models can go a long way towards understanding the function of the software. Briefly, LS-OPT takes an input FE file and runs it using the chosen FE solver. In this case the input file is a keyword file, and the chosen solver is LS-DYNA. LS-OPT varies the value of the material parameters defined in the PARAMETER card within ranges that are specified by the user in LS-OPT. The user also specifies certain outputs to be extracted from the model runs. These can be forces and displacements or stresses and strains, for example, the goal being to extract a model response towards which the parameters are optimized. These outputs are then plotted and compared to some form of input data, in this case an equivalent measured stress-strain or stress-time data curve. The difference in the two curves is calculated using either Mean Square Error (MSE) or through curve mapping, a process measuring the area between two curves. LS-OPT iteratively

narrows the ranges of parameters in the keyword file to minimize the objective function, in this case the MSE of the difference between the input data and the model solution. It will run to one of several termination criteria, either a set number of iterations or else a goodness-of-fit criterion for the data will be reached. The following section discusses in detail how to run a metamodel-based optimization using the successive response surface method (SRSM).

Task Selection

There are two general options when selecting the main task in LS-OPT. The experiment can either be achieved using direct simulation or metamodeling. Both direct and metamodel-based simulations offer Optimization and Monte Carlo analysis, while metamodel simulation also offers robust parameter design and DOE studies, and direct simulation offers Taguchi analysis. There are four further strategies from which to choose when using metamodel simulation, those being the previously mentioned SRSM, Efficient Global Optimization, Sequential, or Single Iteration. A short description of each strategy is visible when choosing. Global Sensitivity Analysis can also be chosen from the “Task Selection” window. Global sensitivities will allow for a nonlinear analysis of the influence of each parameter on the resulting solution. ANOVA is automatically performed with any metamodel-based analysis unless GSA is selected.

In this project, SRSM metamodeling was chosen as some common challenges for direct simulation were expected to be implemented. The notable anticipated challenges included constraints on both the parameters and responses, along with the potential for several local optimal solutions complicating the solution [129].

Setup

The Setup window allows for the ranges of each variable to be set, along with some other settings that were irrelevant to this project. Variables set as constant will be held at a specific value, allowing for a type of model constraint if certain material properties are known. Variables set as continuous will be varied within the ranges that are specified, and with an SRSM evaluation the range of each of those variables will be iteratively shrunk or shifted as an optimal solution is approached.

Sampling

The Sampling window allows for selection of a particular metamodel, an order of the metamodel (linear, linear with interaction, quadratic, or elliptic), and a point selection strategy. There are again some small settings that can be altered in this menu that are not relevant to the studies performed here.

Stage

The Stage dialogue controls how data is extracted from model runs for analysis. The “Histories” tab leads to data that spans the complete range of time of the test, whereas the “Responses” tab is for extracted single values at a specific time. Histories are best used to form the basis of the objective of the LS-OPT experiment. Responses are effective for creating constraints that are treated by LS-OPT as a sort of secondary convergence measure. It is also possible to use an expression to create an objective function from a set of responses. The Stage dialogue also allows for specification of the solver package, the input .k file (or other model file), and the number of processors that can run simultaneously. A 4-core processor would allow 4 simultaneous instances of the keyword file to be evaluated, for example. Other advanced options include compressing the d3plot file outputs and scanning for missing DATABASE cards. This can be useful since depending on the analysis being performed, there can be many different DATABASE cards necessary to a successful OPT experiment, and it is simple to neglect creating just one. This is a mistake that would take several hours or longer to notice, as the DATABASE cards will not be queried until all models in a single cycle have been executed. One other useful tab is “File Operations”, which allows a specific file or files to be copied or deleted after each iteration executes. This is particularly valuable for the ‘d3hsp’ files that routinely grow in excess of 5 Gb file size, and this will cause an OPT experiment to fail if the hard disk runs out of space. The files are non-critical to these simulations and can therefore be deleted, saving an immense amount of disk space.

Composites

This dialogue offers options to set and control the comparison of OPT model outputs to the input data. By comparing each model output to input tensile data through curve matching, such a value can be minimized by area under the curve or by difference between y values. In the case of

comparing Stress-Strain data, a crossplot must be created of the stress and strain data in the Histories tab of the Stage window before it can be compared to input data. As with other sections of the process, there are many other options built into the composites dialogue that are more relevant to other problems.

Optimization

This is the dialog where the necessary composites and responses are chosen to be optimized. If using multiple objectives, the relative weight of each objective can be adjusted. If using one objective, the weight is automatically 1. The response values and their ranges do not have a weight, and in that regard can be considered as secondary objectives. Despite this fact, responses are still very useful to constrain single values within the simulation.

Termination Criteria

The default Design Change Tolerance and Objective Function Tolerance are 0.01. A lower tolerance may be desired in some cases. This dialogue also allows for control of the maximum iterations of the simulation and to choose whether all or merely one of the termination criteria must be met to reach job completion.

Other Settings

When using SRSM, the “Domain Reduction (SRSM)” has no settings that need to be altered. This is also true for the “Termination Criteria” and “Verification.” The job is started with the green triangular “Play” button along the top bar of the LS-OPT GUI. It will then change into a red square “Stop” button. A verification run can be chosen to check that the setup is correct, and in that case only one model will execute. Otherwise, running the job will begin the full slate of models. To view results after one set of “Stage” jobs has executed, “Open the viewer” is selected, to the right of the button to run the job. The viewer allows for viewing of simulation and metamodel histories, and the optimization history and variable sensitivities. As the iterations execute, radial buttons on the “Sampling”, “Stage”, “Build Metamodels”, and “Optimization” will illuminate green to indicate the progression of the job to/through that step. The radial buttons can be selected for more information about the job execution.

5.2. Specific Model Settings

MAT 092 Optimization

The Soft Tissue (Visco) material model was a convolution model with transverse isotropy through a modeled fiber component. In this case, 13 individual model parameters had to be determined, 6 to describe relaxation and 7 to describe the loading behavior. The Hyperelastic coefficients describe stress-strain behavior of the material model, and so it is sensible to use stress-strain data as the input and fit the coefficients accordingly. This meant requesting measures for both stress and strain in the “Histories” dialogue and outputting the same measures using DATABASE cards in the master keyword file. The cross-plot option was then used to create a stress-strain curve output. The stress-strain curve was compared to stress-strain input data. The Mooney-Rivlin hyperelastic model is often used to model ground substance behavior in sclera [92, 130], and so there are some available starting points for those coefficients. The value of XLAM could be identified by inspecting the stress-strain curve and making a determination about the switch between toe and linear behavior, or it could be constrained this way and optimized for a best fit. The slope of the linear region of the stress-strain curve can also be measured and tightly constrained before optimizing. This leaves the Hyperelastic coefficients C3 and C4 to be determined, along with the full set of Prony series coefficients. Once a first optimization run was executed, this OPT routine would be run a second time using the determined hyperelastic coefficients to optimize the viscoelastic coefficients. The viscoelastic coefficients optimization run would be based on a best-fit of the stress-time data curve, since the viscoelastic coefficients control time-dependent model behavior. This two-part strategy was effective but more time-consuming than a single opt routine would be. It is also possible to use multiple dependent modeling stages within a single LS-OPT experiment, and a strategy of optimizing hyperelastic coefficients, then viscoelastic coefficients within the same experiment could have a positive effect on the overall runtime. However, LS-OPT would necessarily still have to execute the same total iterations of the FE model to complete this portion of the job, implying that any time savings would be minimal. Ultimately, the anisotropic nature of the material model meant that it would not be sufficient for anything except tensile experiment

modeling, and even then it would not have a sound theoretical framework, as sclera tissue is largely isotropic in the regions being studied.

MAT 176 Optimization

The Quasi-Linear Viscoelastic material model has the advantage of using fewer total coefficients to fully describe the material behavior. The trade-off of this fact is that the exponential function of strain used to describe the hyperelastic loading behavior tends to be less accurate than the more complete toe and linear region description provided by the MAT 092. Since the MAT 176, QLV model does not require separate parameters describing the toe, linear region, and their crossover region, it is much more feasible to fit all of the coefficients through minimization of the curve fit of the stress-time data. This procedure takes significantly less time than the separate curve fitting for the 13 parameters of the Soft Tissue (Visco) material model. In the MAT 176 case, All 7 coefficients were optimized from the same experiment, with ranges that were developed over several experimental iterations and that varied with each data set. For the Hyperelastic coefficients, initial model runs were performed with one coefficient. Further experiments were performed using a second Hyperelastic coefficient, seeking an improved loading region fit.

5.3. Other Topics

A Note about Viscoelastic coefficients from YC Fung

Fitting of Prony series viscoelastic coefficients can be an efficient method of describing the relaxation spectrum of a material. It must be noted that there are some challenges with using a Prony series description of viscoelasticity. An example is cited in the YC Fung text of three separate sets of Prony series coefficients that could fit a dataset equally well. The point is made by the original author of this case [131] that the issue lies with the extreme sensitivity of the exponents and their multipliers to very small perturbations. Therefore, there will always be some challenge in claiming that any set of Prony coefficients are “the” representative coefficients of some dataset. It can be shown that individual 5 parameter Prony series fits of relaxation spectra will consistently converge to the same parameters using a Levenberg-Marquardt algorithm regardless of the starting values [36].

Different Optimization Quantities (SECFORC vs. D3PLOT)

Two different methods of creating stress-strain and stress-time output curves were pursued. The first method used SECFORC and NODOUT binary outputs, manipulating them to represent the stress and strain of the model. The SECFORC binary output was used to collect the force on the cross-section for the entire model time, and the NODOUT keyword was used to collect the displacement of a node on the displacing face. The stress and strain were then calculated by dividing the SECFORC value by the initial area of the material cross-section and the NODOUT

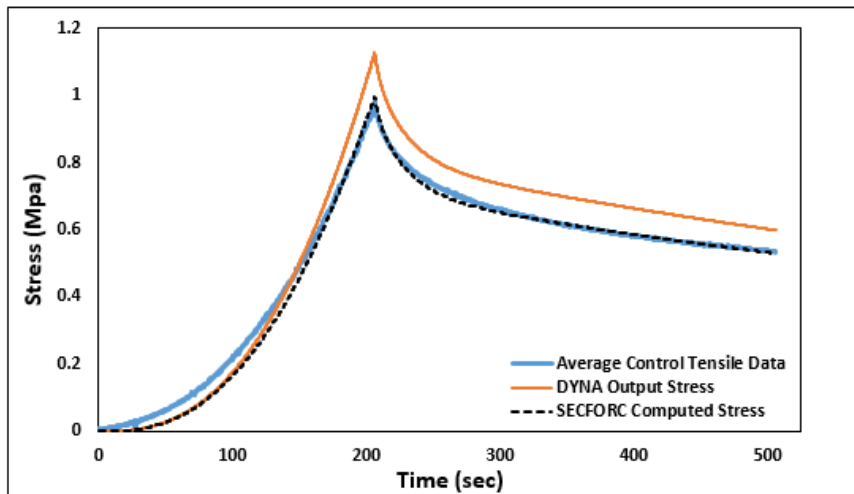


Figure 9: The average material tensile data is plotted against the SECFORC-Computed Stress and the DYNA Output Stress. The method by which LS-DYNA outputs the stress is clearly important in the experimental design.

value by the initial length of the model. These values were a logical and simple method to obtain the stress and strain outputs of the LS-OPT model. It was found over time that the stress value calculated from the SECFORC did not exactly agree with the stress output from LS-DYNA, as

seen when calculating the stress and plotting it with the DYNA output stress in dogbone and cube models. Figure 9 showcases the result of an LS-OPT routine that was done using SECFORC to calculate the stress from the model cross-section. The optimal parameters were then used to output the X-stress from the simulation model in LS-DYNA. The SECFORC –stress is clearly fit to the black dotted line, which represents the collected data. However, the LS-DYNA output stress overshoots the peak stress and is offset from the input data curve by about 77 kPa at 300 seconds, a difference of 11.7%. This clearly indicates that for this material model, it is not appropriate to use the SECFORC output and divide that quantity by the initial cross-sectional area. Further material model fits were performed using the D3PLOT option in LS-OPT to output the x-stress on the x face of the model element.

Some settings had to be changed from the initial setup to accommodate the LS-OPT model running while using the D3PLOT output to report stress. When calculating the difference between the input data and the LS-OPT experimental curves, it was previously sufficient to use a pointwise MSE calculation to determine the minimized quantity. However, a switch to the D3PLOT output stress caused the simulation to stop advancing when calculating the curve matching quantity from MSE. The number of points comprising the MSE calculation was reduced several times to what seemed like a minimum value and the simulation would still be unable to progress past this point. A switch was then made to Curve Mapping (area between curves minimization) as the curve matching algorithm, at which point the LS-OPT experiments were able to run without interruption.

Stress-Strain fit of Stress-Time result

Fitting some of the LS-OPT parameter sets with stress-time curves meant that there would be an implicit fit of the stress-strain output data to the input tensile experiments. It was necessary that the stress-strain tensile data be sufficiently fit by the LS-OPT experiment, so that it could be presented as a good solution for the tensile data. If the LS-OPT fit were to both over and undershoot the target curve at various points to arrive at a minimized curve matching quantity, the fit would not represent a sufficient fit of the input data. The LS-OPT parameters would have to provide both an appropriate stress-strain loading curve and a well-fit relaxation curve to be considered a good fit of the experimental data.

5.4. LS-OPT Parameter Results

LS-OPT Model Results

The LS-OPT best-fit parameter sets for the Soft Tissue (Visco) and the QLV material models are presented in Table 3 and Table 4, respectively. Two QLV Material Model parameter sets are presented in Table 4, one featuring a single elastic response coefficient and the other using two elastic coefficients to define the loading response. Both of these parameter sets had uses while simulating the tissue response to loading.

Table 3. MAT 092 Material Parameters

Parameter (units)	Value	Parameter (units)	Value
C₁ (MPa)	500	S₁ (MPa)	1.625
C₂ (MPa)	500	T₁ (sec)	7.900
C₃ (MPa)	293.89	S₂ (MPa)	2.160
C₄	36.296	T₂ (sec)	12.676
C₅ (Pa)	1.422E+06	S₃ (MPa)	1.347
XLAM	1.135	T₃ (sec)	96.665

Table 4. MAT 176 Best-Fit Parameter Sets

Rate (mm/min)	Treatment	Parameter						C₁	C₃
		G₁(MPa)	G₂(MPa)	G₃(MPa)	β₁ (s⁻¹)	β₂ (s⁻¹)	β₃ (s⁻¹)		
0.5	Control	0.074932	0.055732	0.046246	0.29837	0.04218	0.00097		4361.85
	Genipin	0.089124	0.047466	0.052582	0.42248	0.03182	0.00079		5393.57
	Control	0.125958	0.021090	0.021003	0.45137	0.02527	0.00095	18.3982	5895.91
	Genipin	0.094110	0.014340	0.019772	0.35754	0.02000	0.00064	22.7139	8595.80
100	Control	0.099999	0.036386	0.029018	2.06162	0.08415	0.00198		5265.59
	Genipin	0.108423	0.040964	0.049998	1.57391	0.04696	0.00159		5682.06

Chapter 6: Finite Element Models

The preceding sections have outlined different material model options, the procedures used to collect the uniaxial tensile data and globe displacement data, and the results of that mechanical testing, along with the optimization of sets of FE material model parameters. The present chapter will discuss the different FE models constructed for this project in LS-DYNA. These models are intended to be complementary to uniaxial tensile tissue cross-linking results and perilimbal aqueous vein strain measurements [100], of which the perfusion was described in Section 4.1.1 and the tensile testing was described in Section 4.1.2. Specifically, parameter studies using the whole-globe models can be used to amplify and guide strain measurements like those in [100].

The finite element models built during the course of this project will be cataloged and the purposes they served will be detailed. The FE models described in the following chapter will grow from initial simple models of tensile tests and full dogbone models meant to confirm the performance of the material model, into models attempting to re-create the conditions of perfusion IOP tissue loading, and then on to globe section models meant to produce insight into the tissue stresses and strains during perfusion IOP loading.

6.1. Models for Optimization and Validation

Finite element models were explored and developed with the overarching goal of furthering an understanding of the sclera behavior, especially as it relates to the embedded aqueous veins. First, it was necessary to develop a model for property identification simulation with LS-OPT. LS-OPT is a companion software package to LS-DYNA that can perform various optimization routines and that offers a robust set of options for completing them. LS-OPT was used in [80] to fit parameters for material model 092 in LS-DYNA to simulate ligaments of the lower leg during pedestrian vehicle impacts. LS-OPT was also used in [132] to fit parameters of a model for aortic tissue, and features an extensive description of LS-OPT theory. The property identification was informed by collected tensile relaxation data at various strain rates. The length of the tensile relaxation tests (approx. 300 seconds) and the number of property identification iterations (often

10-15 iterations) made it necessary that any finite element model for property identification must run quickly. A simple finite element model composed of a single element was therefore developed to allow the robust simulation of the tensile relaxation tests. This model was used to run the LS-OPT parameter identification.

Tensile Dogbone Model

A finite element model of a tensile dogbone gage length was created with the goal of developing a simulation in good agreement with the collected tensile relaxation data. This model began as a tensile gage length model (a rectangular prism) of approximately 8-13 individual cuboid elements. These simple models were used to simulate the output of tensile elongation experimental data, eventually being implemented to run in LS-OPT with the goal of finding material parameters. The model experienced significant hourglassing effects, and the simulation model for LS-OPT was replaced with a single cube element with side length of 13 mm to shorten simulation runtime. The side length was equal to the gage length of the tested TE samples. The simple tensile gage length was then implemented as a check for the LS-OPT data fits, and in order to serve this purpose, it was gradually replaced with a more and more complete tensile dogbone model. This eventually led to the creation of a full tensile dogbone model with BCs consistent with the TE tests performed in the lab. Initial iterations of the tensile dogbone model did not successfully demonstrate agreement with the TE experiments, and the extreme elongation conditions of a TE experiment meant that significant hourglassing still occurred. A decision was made to explore stiffness hourglass control formulations, and it was found that such a control measure could effectively prevent the hourglassing effects that had persisted.

Single Element Model

The single element model was implemented with a goal of running the most rapid LS-OPT experiments as was feasible, in this case by minimizing each model iteration's runtime. The element was built with 13mm sides to have sufficient volume so as to avoid the development of any hourglass deformation modes, and since theoretically any stress calculation will naturally counteract the significantly larger cross-sectional area. It was anchored along its negative X face using a single point constraint (SPC) at each of the corner nodes. A displacement in the positive X direction was applied using a prescribed motion at each of the nodes of the positive X face.

The PARAMETER card was invoked to allow LS-OPT to vary the material model parameters. An elastic test material was included to perform verification runs before using the model in LS-OPT.

Tensile Bar Models

A series of tensile bar models were developed to approximate the behavior of the tensile elongation material samples to applied stresses or strains. Though they were initially developed to be implemented with LS-OPT experiments, various challenges led to the implementation of the simpler single element model for those experiments. These models were then also used to attempt to validate the LS-OPT results and to better understand the effects of applying loads or displacements to this basic structure. These models had cross sectional dimensions of 1.5 x 1.6 mm, and were mostly 13 mm length, although a few test models were of different shorter lengths. Most of the tensile bars were coarse models where the cross-section was spanned by a single element. In one case, the cross-section was created from 2 elements in each of the y- and z-directions. Almost every model consisted of 13 elements in the x-direction, although two models were created with one and two elements, respectively, in the x-direction. All models included SPCs applied at the nodes of the negative x face of the model and prescribed motions on the nodes of the positive X face. These models also included PARAMETER cards, and contained multiple MATERIAL cards, including an elastic test material. Viscous hourglass control formulations were applied to these models, which had no effect on problematic deformations that continued to occur. The work with this type of model was done before stiffness hourglass deformation control was explored and found to be very effective in this role.

Dogbone Models

A series of tensile “dogbone” specimen models were created to validate the material parameters that were being produced for material models by LS-OPT. Though the simple cube model implemented in LS-OPT was consistent with the extension length of the tensile dogbone samples and the calculation of stress meant that its cross sectional dimensions should not have an effect on the result, it was important to seek a model of the data collection experiment as a way to verify the material model’s performance. A series of FE models that could accomplish this goal were generated. They all had in common a gage length approximately equal in dimensions to the

average sample dimensions, 13 x 1.5 x 1.5 mm. Beyond that consistent aspect, many different solutions were tried to generate a quality, representative FE model that was also light on CPU resources and used sensible boundary conditions to demonstrate a converged material model solution.

Some of the first models that were developed attempted to simulate the entire shape of the tensile dogbone. Such a model was constructed from measurements of the test sample cutter, with a gage length of 13 mm and a full length grip-to-grip of 31 mm. It was taken as 1.5 mm thick, with a 1.5 mm gage length width and a 4.5 mm grip width. A single hexahedral element was used through the thickness of the model, and a single pentahedral (degenerate hexahedral) element was used for the corners of the grips narrowing to the gage length. The elements of the grips were 1.5 mm cubes, while the elements of the gage length were 1.0 x 1.5 x 1.5 mm. ELFORM 1 was used to calculate the element stresses, and a viscous hourglass control was imposed in an attempt to prevent the development of hourglass deformation modes. A Viscoelastic material model and elastic test material model were both inserted to be used as necessary. A boundary condition SPC was imposed on all nodes of the stationary grip, while an appropriate displacement condition was imposed on the nodes of the opposite grip. A DATABASE card was included to govern the frequency of d3plot file outputs (BINARY_D3PLOT).

Following the development of this model, a series of experiments were undertaken to solve a consistent hourglassing deformation. The solutions attempted were to vary the material model parameters, a rebuild of the FE mesh within LS-DYNA as opposed to Hypermesh, and varying levels of and implementations of HG viscous control. Following these attempts, varying ELFORMs were implemented to visualize if any such calculations could prevent the development of hourglass deformation modes. None of the applied ELFORMs prevented the ultimate failure of these models, though some did prolong its stability considerably.

After these attempts, a series of different experiments deconstructing and reconstructing the tensile dogbone model were performed, investigating the theory that something about the geometry of the shape was having a strong effect on the hourglass deformation and chaotic model failures that had been occurring. None of these shape changes were able to prevent hourglass deformation, although there were many interesting explorations of partial dogbones that would end up contributing to the final design of the tensile dogbone. A notable model created during this period was a dogbone model that removed the dogbone grips up to the

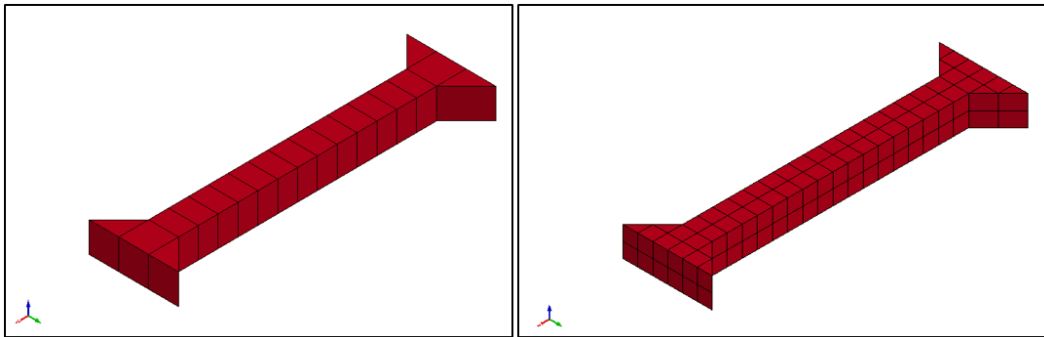


Figure 10: Dogbone FE Model for applying displacement boundary condition orthogonally to the surface of one end while fixing the other end. Two different mesh densities are shown.

shoulders, so that there was a gage length mounted to two dogbone shoulders. The boundary conditions applied to the vertical faces of this model removed some unnecessary complexity, and also simplified the region to which the BCs needed to be applied.

The previously described trimmed dogbone model (model including gage length and shoulders) was later implemented with very slight stiffness hourglass control to effectively simulate the tensile stress relaxation experiment upon which material parameters had been based. The two vertical grip faces were now used to apply the SPC and displacement boundary conditions at each node of the face. A finer mesh is also shown here, where the elements of the shoulder segment were 0.75 mm cubes and the elements of the gage length were 0.764 x 0.75 x 0.75 mm, with a slightly longer side length in the x direction to fill it with approximately consistent elements. The coarse mesh used 1.5 mm cube elements in the shoulders and 1.0 x 1.5 x 1.5 mm elements in the gage length. The DATABASE card was set to output model data every tenth of one second. ELFORM 1 was used for these model runs.

6.2. Development of Whole-Globe Models

Although these models are collectively termed “whole-globe” models, there are several differences between them and a fully meshed eye globe. The models with spherical curvature assume the globe to be a perfect spherical shape. Apart from that simplification, it is a whole globe model, though the use of symmetry in the creation of the FE mesh permits only a portion of the actual globe to be modeled in LS-DYNA, thereby greatly reducing computation time. The limitation of this approach is that mechanical behaviors due to deviation of the shape from spherical cannot be captured by the model. For the remainder of this document, this modeling approach will be designated the "whole-globe model”.

Simplified Chunk Models

Simple chunk or segment models were explored next with the intention of relating model behaviors back to the LaPlace Law of thin-walled spherical pressure vessels. If this model could show such behaviors, then it would be seen as a suitable direction for continued construction of increasingly complex FE models of a segment of a porcine globe. Unfortunately, these models returned largely incorrect model results due to the use of an element formulation that reported lower stresses. This resulted in this subset of models being discarded for a period of time until the element formulation was identified as the culprit for these erroneous results.

These models started as a 1 x 2 x 2 mm rectangular prism constructed from 32 0.5 mm cube elements. Assuming a 12 mm radius for a human eye [133], the 2 mm segment of eye tissue would be about 2.7% of the full circumference, or about 9.5% of the circle. To keep this model simple, it was chosen to not use any curvature at this time. The model was constructed with full SPC boundaries on all the nodes along each vertical face, with a load approximating IOP applied to the bottom surface. To begin, only two of the vertical faces SPC boundaries were applied, those perpendicular to the Y axis. The pressure applied to the bottom face was taken from a

perfusion experiment performed on a full porcine globe. The pressure was applied in units of Pascals and seconds. A steady pressure change of 4.828 mmHg (643.7 Pa) was applied to the globe over a period of 9.727 minutes (583.6 sec). These were the parameters used to apply the loading. The resultant loading proceeded at 1.103 Pa/sec. The PARAMETER card was used to apply values to the MAT_176 card that had been determined using LS-OPT. The material parameters would continue to be refined, but these parameters were an acceptable “first-cut” set.

ELFORM 1 vs. 2 problems

The constant stress solid element formulation (the default formulation, ELFORM 1) was used for the first iteration of this model. A problematic early output of this model led to troubleshooting that ended with the

application of a fully integrated element formulation. This ELFORM would persistently understate the stresses as compared to simple physical models of the structure, leading to confusing and borderline nonsensical results and much needless problem-solving. It was eventually found that ELFORM 1 would produce much more appropriate stress results in most cases. The best current explanation for this problem is that with 0.5 mm cube elements in a 4 x 4 x 2 layout, the constant stress elements were much too large to capture the behaviors effectively, whereas the fully integrated element formulation could offer more complete analysis of the stress state. However, as the ratio of element edge length to model edge length dropped from 50% to closer to 10% or less in the smallest model direction, the fully integrated elements quickly began introducing errors. Further, their precision was not relevant as the elements grew smaller relative to the complete structure. The same faulty model composed of 32 cube elements was increased to 256 cube elements, and the warping behavior that caused the initial investigation was not apparent in the 256 element model.

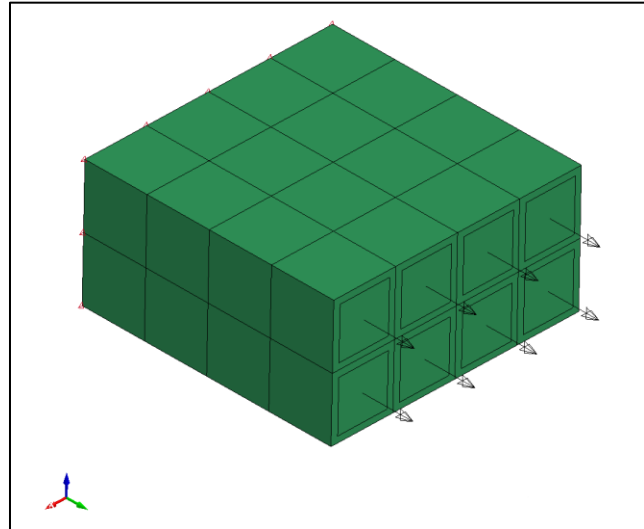


Figure 11: a flat segment of tissue model with applied wall pressures as boundary conditions (arrows)

Chunk Model Boundary Condition Variations

Many boundary condition variations were attempted to improve the output of the giant element chunk model. One of the working theories was that applying a loading condition equivalent to the resultant load in the LaPlace Law sphere hoop stress from an internal pressure. The LaPlace law states that the hoop pressure σ will be equivalent to $Pr/2t$, where P is the internal pressure, r is the radius of the sphere, and t is the wall thickness. These values were simple to derive, and so this stress was applied to the vertical walls of the giant models in many different configurations. Some interesting choices included applying $Pr/2t$ BCs to each vertical face and anchoring one node at the top of the model to prevent the imposed IOP from accelerating the model in the +Z direction; applying the $Pr/2t$ load spread out across nodes as a sum of forces instead of as a pressure across element faces; and adding springs of different spring constants along the vertical edges to gently constrain the model. All of these models were motivated by attempting to fix the stress discrepancies that were later discovered to be a result of ELFORM 2, but they did result in interesting investigations into the behavior of the chunk model under different boundary conditions.

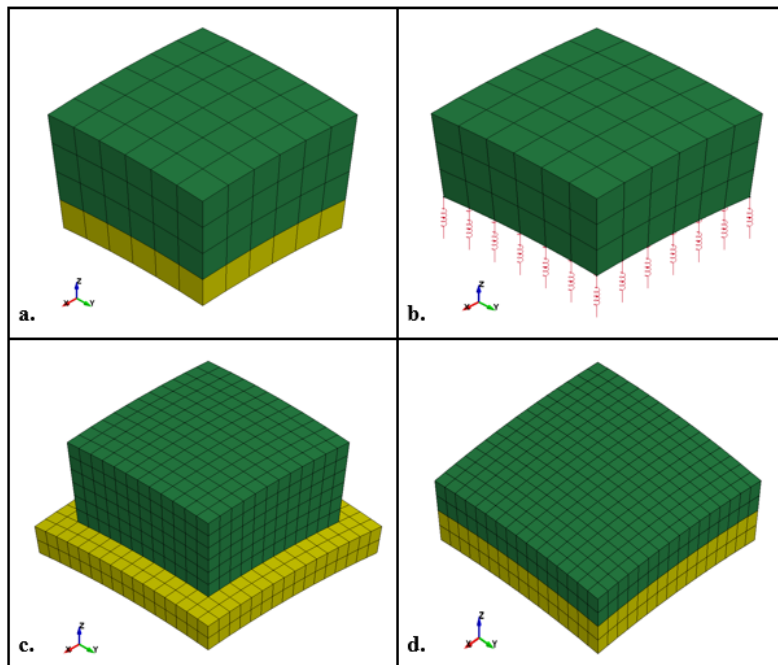


Figure 12: A series of "forcing element" FE models meant to investigate methods of applying IOP loading to the internal surface of a globe segment

Forcing Element Models

In pursuit of a solution to the problems being caused by ELFORM 2, a series of models were created using a layer of elements underneath a tissue chunk model to see if using so-called "forcing elements" to induce the IOP loading could improve the situation. While ultimately unsuccessful in the same way as the chunk models were, this was again an interesting departure into

unconventional methods of applying boundary conditions. The forcing elements were imagined to be a solid material that pressed on the inner surface much like aqueous or vitreous humor. The elements had material properties similar to water in terms of density, and a variety of young's moduli (E), both stiffer than and softer than the tissue elements, were tested for this model. Some of the different model configurations are pictured below. They include the starting model (a), a model with springs and an applied stress directly to the $-Z$ face (b), a model with the forcing elements extended out from the edge (c), and a model with a thinner tissue layer that sought to decrease "wall" thickness and improve correlation with the LaPlace law for thin walled spheres (d).

These FE models used a variety of boundary conditions to fix and support the tissue and forcing elements. Two symmetry constraints were imposed through the center of the tissue elements, fixing them to have no translation or rotation out of the two vertical midplanes. Since the pressure was applied to the tissue elements via displacement of the forcing layer, there was no need to anchor tissue elements in the Z direction and prevent them from flying away. In the case of the springs in b. above, the pressure was applied directly to the tissue elements of the $-Z$ face and they were restrained by the springs. The QLV material model was used for tissue elements and a linear elastic tissue model was applied to the forcing elements. The displacement was imposed on the bottom surface of the forcing elements and the value of E was calculated and tweaked to deliver the approximate IOP load to the bottom tissue elements. Loads calculated as the LaPlace Law equivalent pressures for the targeted IOP load were also applied to the 4 vertical walls of the model.

Vein-in-Tissue Rectangular Prism Chunk Models

A series of vein-in-tissue models were constructed to begin to explore the relationship between a vein structure and its surrounding tissue region. Embedding a cylinder structure into a rectangular structure with a coarse mesh density is a challenging task that requires compromise on mesh homogeneity or on vein shape, and so these meshes offered a first-cut look at the structural relationship. A series of mesh densities were built, pictured below. The mesh in a.

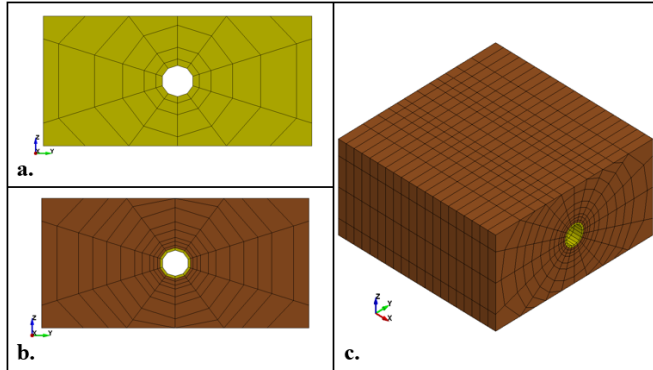


Figure 13: Vein-in-tissue models with increasing mesh densities. The thin vein elements limit the timestep size of the FE Model.

neglected to incorporate a vein structure to minimize runtime, and so was built as a tissue region with a decagonal hole through the center of the YZ face. The mesh in b. had the same 10 sides to its hole, but twice as many elements in each radial direction and was built with a thin vein inclusion.

The vein hole in a. had a radius of 0.12 mm, and the vein in b. had a wall thickness of 0.02 mm, reducing its inner diameter to a 0.1 mm radius. The model in c. was made with twice as many elements composing the circumference of the vein, and 20 elements created a much better cylindrical shape. All three meshes were extremely radially symmetric, with elements radiating out from the vein structure creating the appearance of a spider's web. This structural technique of embedding a vein would be used later in a larger vein/tissue model.

The vein hole in a. had a radius of 0.12

The boundary conditions to fix this model were applied to the positive and negative XZ-faces, applying full SPC conditions to each node along the faces parallel to the axial direction of the vein. The remaining faces were left free with the intention of allowing the vein structure to deform freely. The same QLV material model was applied to both the vein and tissue model parts. This effectively defeated the purpose of including a unique vein part, and would be changed in later models. The creep load of 1.103 Pa/sec was applied to the bottom surface of the tissue material, and a load equivalent to half of the IOP load, 0.55 Pa/sec was applied to the vein internal surface when present. The models were run to a termination time of 50 seconds to show significant deformation without using excessive runtimes.

6.3. Models of Whole-Globe Response to IOP

Hoop Models

A quarter hoop and full hoop model were both created to explore the application of IOP as the only loading condition. Rings of tissue material were used to minimize the size and runtime of each model step. If this model was shown to generate reasonable strains and stress responses,

then it would make sense to continue on to a larger tissue segment. The quarter and full ring models are pictured below. Each ring was about 1 mm thick with a radius of 12.5 mm. The model was 3 elements thick, 6 elements wide, and 60 elements made up the 90° arc. The elements

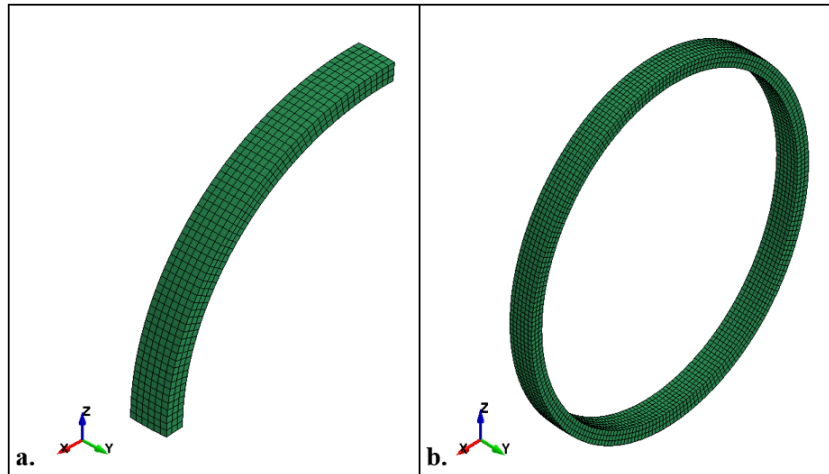


Figure 14: Quarter and Full Hoop FE Models exploring the application of IOP in a radially balanced manner.

varied in size based on their location in the model, but they averaged approximately 0.33 x 0.32 x 0.32 mm (r, θ , z).

Three symmetry boundary conditions were applied to constrain the models. For the quarter ring model, the XY-planar bottom face and YZ-planar top face were constrained in their respective planes, and an XZ-plane symmetry was imposed between the central element layers. The same boundary conditions were applied for the full ring model, with the XY- and YZ-plane BCs extending across the ring to include those opposite nodes as well. The IOP load was applied to the internal surface of the rings. The pressure and load time were in line with the previous perfusion experiment data, 643.7 Pascals over 583.6 seconds. QLV and elastic material model cards were included in the keyword file. ELFORM 1 was used for the full hoop model, while ELFORM 2 was used for the quarter ring model. The results of this model in terms of hoop stress were sufficient to merit a pursuit of a series of larger sphere segment models.

Eighth Sphere Model

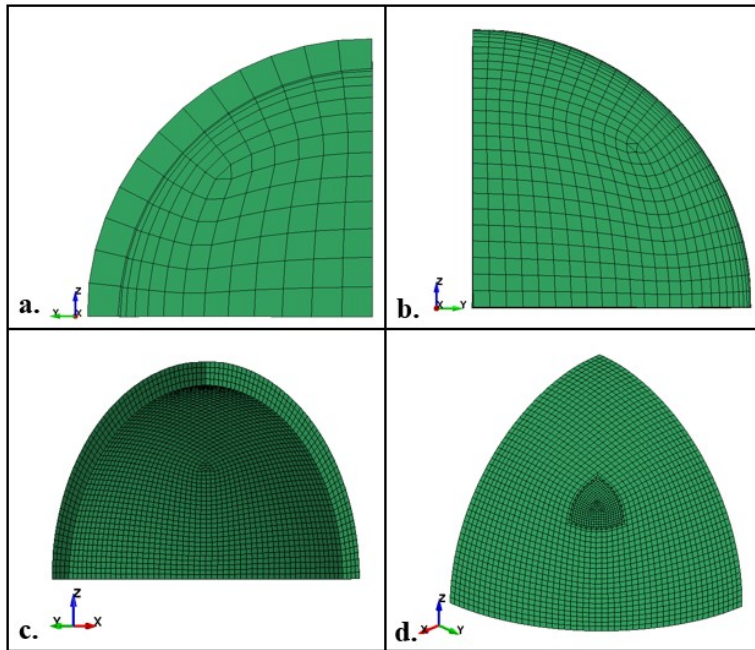


Figure 15: Eighth Sphere FE Models of increasing density. Note that from c. to d. only a small central region of elements was further reduced in size, with the hopes of keeping computational time under control.

model in c. was composed of 0.375 mm cube elements, and the finest mesh in d. was mostly 0.375 mm cubes with a central section of elements that were around 0.15 mm cubes.

These models used the same symmetry boundary conditions as the ring models. The XY, XZ, and YZ planes that subsect the theoretical sphere into eighths were all fixed to not displace or rotate out of their planes. In this way, the spherical region could only inflate outward. The same IOP load of 1.103 Pa/sec was applied to the interior surface of the model. The elastic material model was used to test each model during development and verify the boundary conditions. The complexity of this the c. and d. meshes forced the switch to MPP-DYNA, which does not substantially affect the keyword file formulation. During this switch, the loading time was decreased by a factor of 10 to enable a full 4.8 mmHg pressure change within a shorter simulation period. The IOP load applied to from that point on was 11.03 Pa/sec. ELFORM 1 was used for all of these meshes. No hourglass deformation control was necessary for these models. The PARAMETER card was used to apply the QLV material model coefficients.

A series of eighth sphere models were created with meshes of increasing complexity in an attempt to show good agreement with the LaPlace law hoop stresses. The coarser models were executed using the Shared Memory Parallel (SMP) LS-DYNA distribution, while the finer models were run using Message Passing Parallel (MPP) LS-DYNA on a Linux computing cluster. Model a. used cube elements with side length ~ 1.5 mm, b. used mostly cubes of 0.75

Connecting Meshes of Different Density

For the model d., a section of extra fine mesh was inserted into the center of the model. This was done to include a region of even finer mesh without having to use an entire eighth sphere mesh at that element density. However, this inclusion required a meshing solution to be developed to connect the finer and coarser elements. A picture of that solution is provided here. Different colors were imposed and elements were made transparent for clarity. It was necessary that the linking elements connect four smaller cube elements to one large cube element, shown here in yellow and red, respectively. A solution involving tetrahedral elements would require the

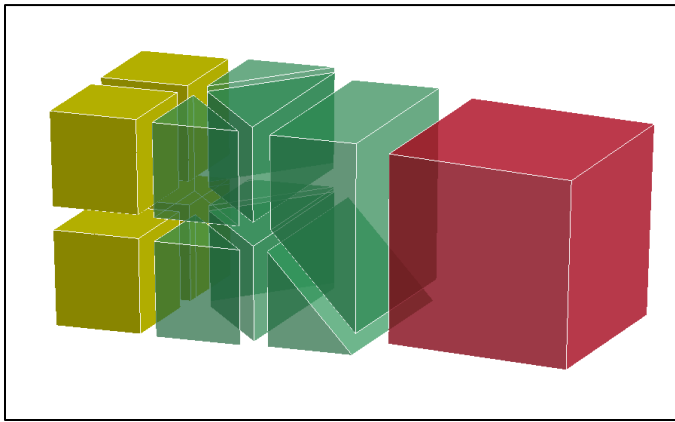


Figure 16: method for linking hex elements of different sizes using only valid 3D element shapes.

splitting of the large element face in some way, and so those were not feasible.

Square pyramid elements are not supported in LS-DYNA. Therefore, the only available elements for this solution were the hexahedral and pentahedral elements depicted here. The triangular prism layer proximal to the fine mesh

reduces the four element faces on the left

to only two on the right, and the two elements connecting them to the coarse mesh element were devised to reduce two element faces into one. This solution provided an easily repeatable motif that can tile around the finer mesh in the center of the model and connect it fully to the coarser mesh of the surrounding region. It was employed again in a later model that sought to use a similar inclusion of finer mesh. In the eighth sphere model, the average stress of a sample of the finer mesh region was 9.5% higher than that of a similar sample in the coarser region. The experiments performed here do not allow for the effect of increasing the mesh density of separate models to be separated from the effect of having two connected densities in the same model. In either case, this structure allowed for the investigation of a finer mesh density than otherwise would be possible, with the material model complexity combined with the decreasing mesh density significantly increasing the model runtimes.

Sphere Segment Chunk Model

With the general successes of building and refining the eighth sphere models, a rectangular spherical segment model was designed to be embedded with a vein structure. A picture of that

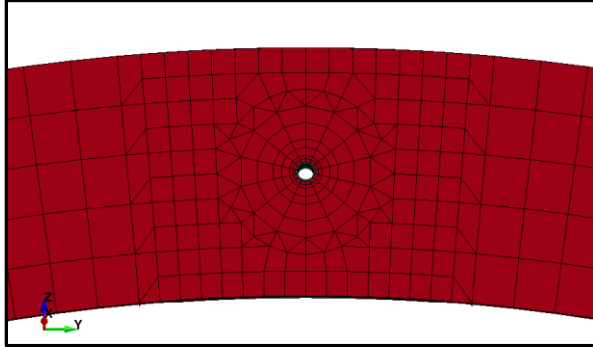


Figure 17: highlighting the region surrounding the vein structure, using the radial element orientation from previous chunk models to surround the vein.

model with and without a vein is seen here. The faces perpendicular to the vein openings were flat, but the other two faces curved along their length, as can be seen of the face in a. approximately perpendicular to the +y direction. The vein is represented as a tube that runs through the center of the model's midplanes. The model spanned 43.6° (0.76 rad) in both the θ and ϕ directions. This segment comprised about 5% of a sphere's total surface area. The larger cuboid elements of this model were 0.3 mm on each side, and the finer hex elements were approximately 0.15 mm on a side. The region surrounding the vein within a 0.5 mm radius was built from radially oriented elements to incorporate the shape of the central vein without breaking element connectivity. An enhanced view of that region is shown here. It is apparent that this region was built from the lessons and knowledge gained by building the earlier vein-in-tissue chunk models. The

radial elements were carefully designed to connect to the regular cuboid elements and they created an overall clean model

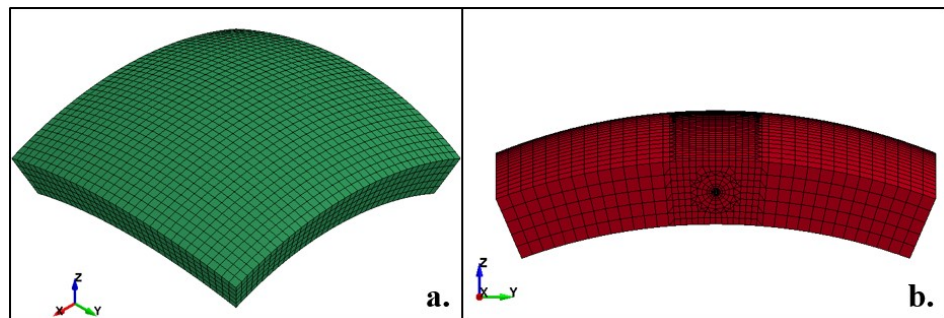


Figure 18: Sphere segment chunk model, a. without vein structure and b. with vein structure.

design, minimizing mesh heterogeneity while also incorporating a very small vein structure into a much larger tissue region. The vein in this model was 14-sided and had a radius of 0.05 mm ID, half of the radius of the previous vein-in-tissue model. The 14 sided cylindrical structure struck a balance between the 10- and 20-sided vein models of the earlier models. At this reduced circumference, the 14-sided vein was sufficiently circular in its cross-section. The two curved

model faces that are approximately parallel to the axis of the vein were fixed with symmetry planes so that they could only expand in the direction of applied IOP. This condition was meant to duplicate the eye expanding outward with increasing IOP. Due to the unique curvature of these sides of the model, 72 local coordinate systems were required to create this boundary conditions along these edges. The surfaces perpendicular to the vein axis were flat and only required one local coordinate system each to be fixed in the plane perpendicular to the expansion direction. The IOP load of 11.03 Pa/sec was applied to the bottom surface, and a proportional loads of either 50% or 63% were applied to the internal vein surface. Two versions of the QLV material model card were inserted to allow for different QLV properties to be assign to each of the vein and the tissue, although complete model experiments were only ever performed with the vein modeled as linear elastic. The PARAMETER card was used to inform one of the QLV material models, and the other QLV model was somewhat arbitrarily set to return only a fraction of the first model's response by reducing the coefficients of the relaxation function (G_i) and the coefficient of instantaneous elastic response (C_3). Two linear elastic material model cards were also created.

SIDR Pre-Loading

As the model was being developed and tested, it became apparent that applying the loading conditions of 1.103 Pa/sec for 583.6 sec would simply take too long. Further, this pressure rate of change would apply 4.83 mmHg of pressure to the internal surface over that time period, equivalent to around 9.7 minutes. While that is accurate to a portion of a perfusion experiment, our research group had collected and analyzed vein strains for a perfusion experiment where the pressure reached 18 mmHg. To reach such a pressure at the quasi-static loading perfusion rate would be even more unrealistic. Therefore, a solution to pre-load the material segment to a predefined pressure state was pursued. This tool is called Stress Initialization by Dynamic Relaxation (SIDR) in LS-DYNA. This process is invoked by setting an SIDR flag in the DEFINE_CURVE card to 1 or 2. When set to 1 the curve will be used for stress initialization, and the loading will be applied in a "pseudo-time" period and then the SIDR will continue until a series of convergence criteria are met. In these sphere segment models, the SIDR loads were imposed from 0-1 "pseudo-time" and then the SIDR process would progress until convergence

was achieved. A “relax” file is produced during this process which can be used to monitor the SIDR progress through parameters such as distortional kinetic energy and convergence. It is accessed through the ASCII database on the associated d3plot file in LS-PrePost. When convergence is achieved, a file called drdisp.sif is produced that contains information about nodal geometry and rotations, allowing for an abbreviated preloading process to be invoked using a CONTROL_INITIAL_RELAXATION card. This abbreviated preloading process is called “initialization by prescribed geometry”, and it is done by setting the IDR flag to 2 instead of 1. IDRFLG can also be set to 5 for an implicit analysis.

An experiment was performed to evaluate the efficacy of preloading with SIDR. A model with 11.03 Pa/sec loading for 58.36 sec (for a total of 643.7 Pa = 4.8 mmHg) was run in increments of 643.7 Pa. The next model would then have an applied SIDR load to the peak stress of the

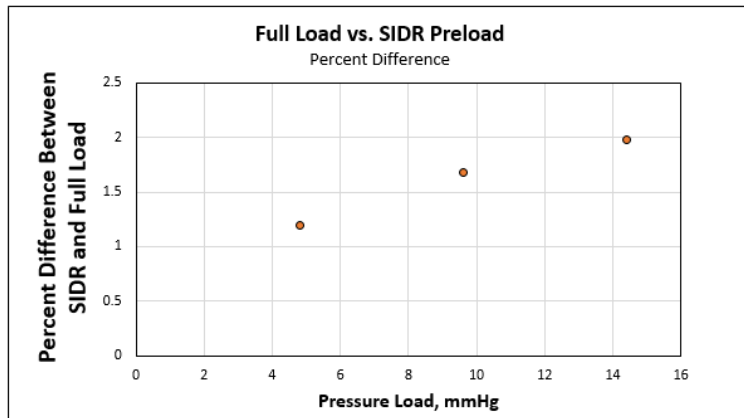


Figure 19: Plot of percent difference between SIDR load and conventional load at $t = 0$ s. The difference increased for each higher SIDR load applied, but was still just under 2% difference for the third preload to 14.5 mmHg.

previous model, then it would run for a further 643.7 Pa. In this way, 19.2 mmHg loading was applied to the model over 4 separate runs. After each SIDR preload, the maximum principal stress (principal stress 1, PS1) value at 0.0 sec was compared to the peak PS1 of the previous run. In this way, the difference in applying the load over

time and preloading the models was evaluated. In each case, the preload value was between 1-2% less than the full loading value of PS1. A chart of the percent differences is shown here. This demonstrates that there is little difference between the SIDR loading-induced model stress and the model stress that occurs due to full loading of 643.7 Pa for 58.36 in-model seconds. This evaluation proved the value of using SIDR preloading as a tool to shorten model runtimes in this particular case. It is best to evaluate the quality of such a solution on a case-by-case basis.

6.4. Validation Model Convergence Results

Dogbone Model Convergence

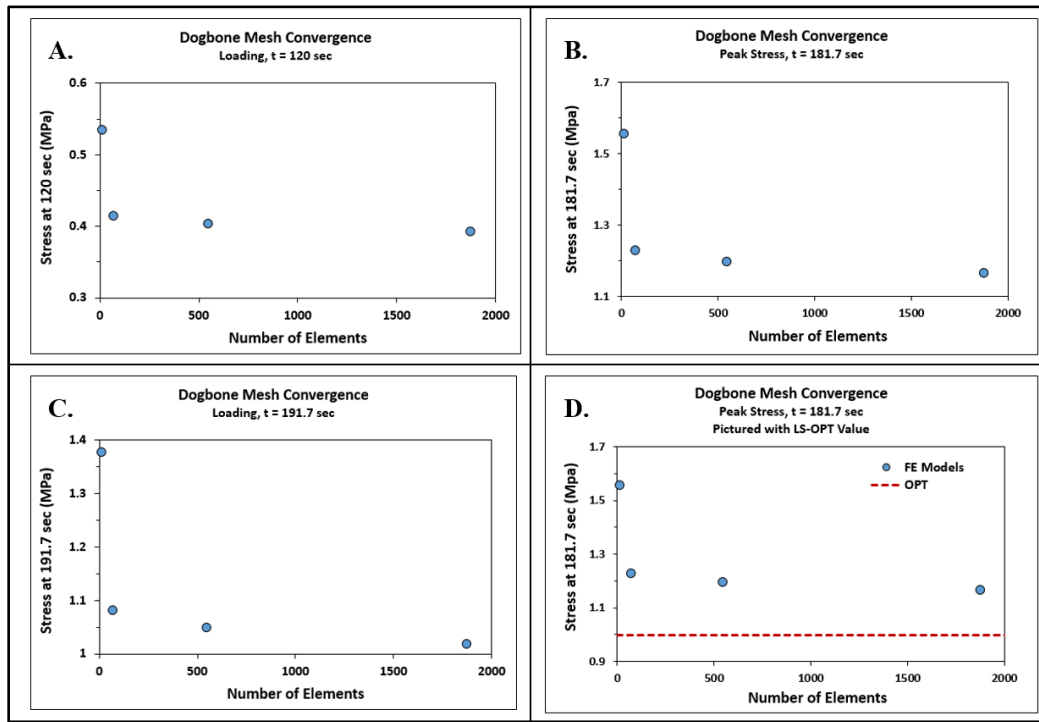


Figure 20: a., b., and c. show the convergent behavior of the dogbone models with increasing mesh density at different times, while d. demonstrates that the values are not converging to the predicted LS-OPT value.

Plots of the dogbone mesh values at three different times are provided in Figure 20. These stresses are seen to converge for each displayed time. Figure 20d shows that the values do not converge to the LS-OPT fitted value, which was demonstrated to be largely an effect of measures implemented to control hourglass deformation. The convergence of these dogbone mesh models at each time demonstrates the consistent convergence of the dogbone models across the entire time of the test.

Another plot presented in Figure 21 offers the explanation for the non-convergence of the model values to the LS-OPT value in Figure 20d. Figure 21 shows the effect of the HG coefficient upon the overall convergence of the stress value to the fitted model. The stress values in this chart are taken at $t = 25$ s for each case. Although the chart shows HG coefficient outputs from 0.001 down to 0, HG values below 0.001 caused element failures later during the experiment. The x-stress in the dogbone model with no HG control was only 2.5% greater than the x-stress of the equivalent

LS-OPT model output at $t = 25$ seconds. Due to the element failure problems at lower HG coefficient values setting a minimum value on the amount of HG control that must be applied, it was determined that a dogbone x-stress value converging to a consistent level (as in Figure 20 a.-c.) would be a sufficient indicator of model quality.

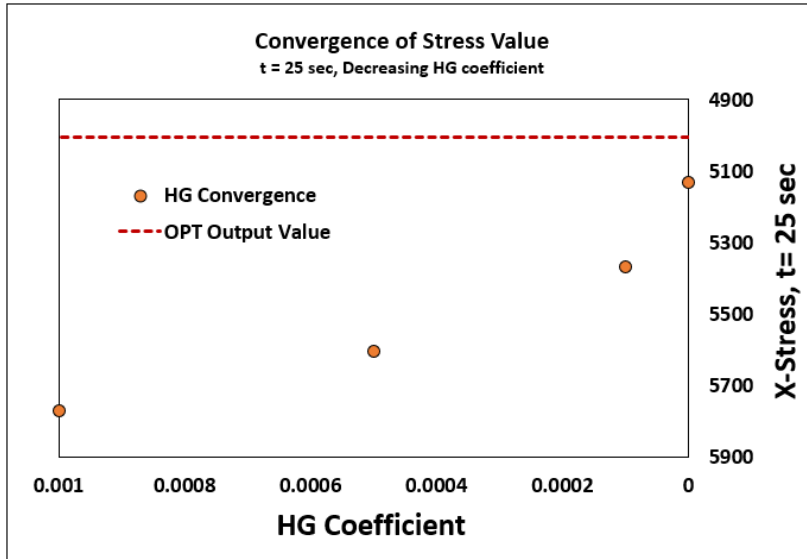


Figure 21: The value of the stress at $t = 25$ s can be seen to grow closer and closer to the LS-OPT predicted value as the HG coefficient drops to zero. However, it never reaches the predicted value.

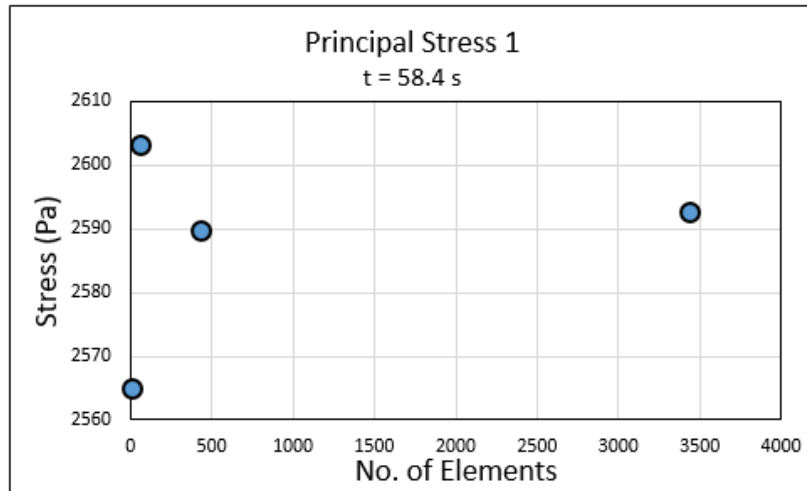


Figure 22: Convergence of maximum principal stress value in eighth sphere model with increasing mesh density.

Eighth Sphere Convergence

The convergence of the eighth sphere model was measured with average stress values from a consistent region of increasing mesh density. The region in the center of the model was chosen since it contained the finest mesh density in its final iteration, and could therefore offer the most points to demonstrate a converging value. Maximum principal stress was measured at 58.4 seconds, shortly after the loading of this model was completed. As there were only four distinct mesh densities run, a trend was only beginning to emerge. However, it is apparent that these values are consistent and already tightly clustered near 2.6 kPa. Charting the minimum principal stress yielded similar results, with values clustered within a 20 Pa range. The eighth sphere model wall stresses generally demonstrated the LaPlace Law $\sigma = Pr/2t$, as an applied pressure of 644 Pa yielded a principal (hoop) stress of nearly 2.6 kPa, aligned with the LaPlace prediction of 2.7 kPa.

6.5. Whole-Globe Model Parameter Sweep Results

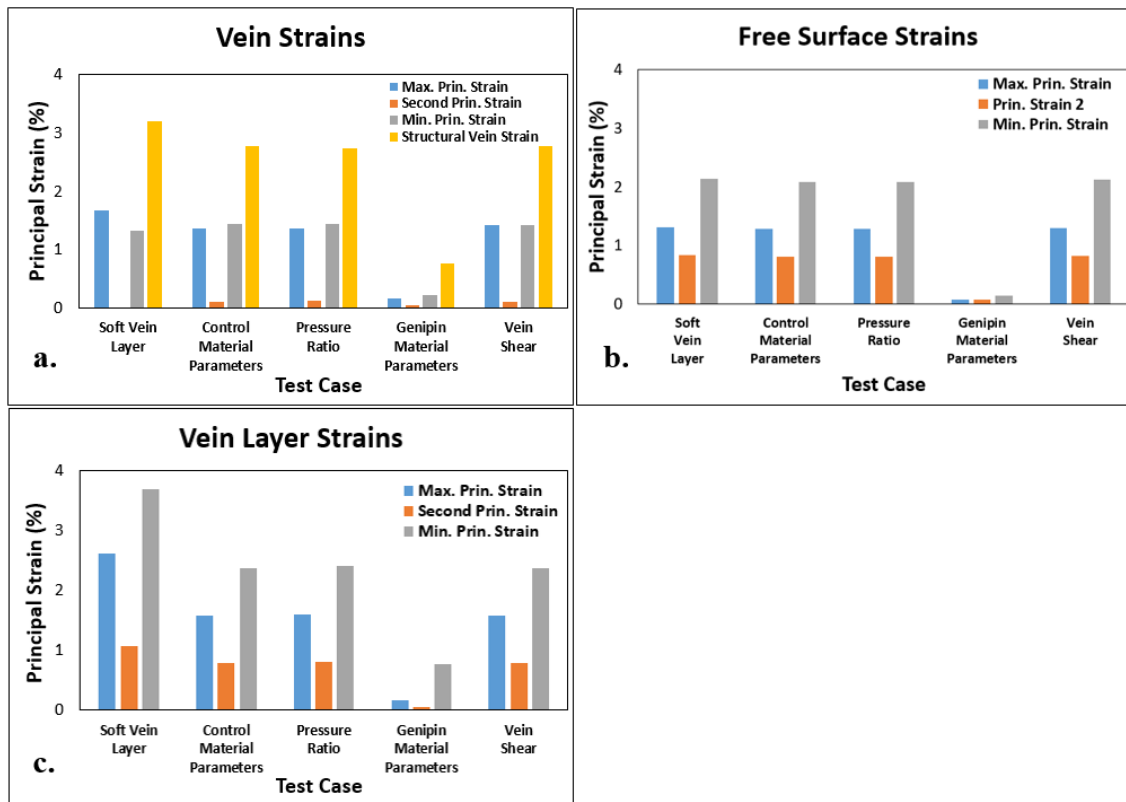


Figure 23: Tissue chunk model strains for a. the vein, b. the outer surface of the globe model, and c. the layer of elements surrounding the vein. In a., the “Structural Vein strain” is a measure of the change in diameter of the vein, meant to reflect the amount of deformation the vein as a whole experiences during IOP loading.

The chunk model strains are presented in Figure 23. The strains of the vein elements are presented in Figure 23a. The strains measured at the surface layer of the chunk model are presented in Figure 23b. as the “Free Surface” strains. The strains in 23c. are taken from the single layer of elements immediately surrounding the vein, called the “Vein Layer” strains in the chart. In Figure 23b. and c., the strains are presented in the three principal directions. The minimum principal strain is presented as a positive value to allow the bar charts to be more ordered, but they were negative values and the minimum principal strains are exclusively compressive. In Figure 23a., a fourth strain measure is presented, referred to here as the “Structural Vein Strain”. This structural vein strain is a measure of the change in diameter of the vein in the thickness direction at the center of the chunk model, and was evaluated as $\Delta d/d_0$, where d represents the diameter. The structural vein strain is also compressive in all reported

cases. The structural vein strain is relevant to any imaging data cases where the shape of an aqueous vein under IOP deformation has been considered, and can offer a good benchmark against that type of data collected in perfusion experiments.

6.5.1. Discussion

Tissue Strains and Comparison to Published Results

The deformation gradient of sclera *in vivo* has been extensively measured and modeled in an effort to better understand the progression of eye disease. In studies where deformation is measured, the IOP is commonly also reported to create an analog stress-strain relationship. Sclera strains are often measured or studied in an effort to understand the displacements that occur around the optic nerve head. When strains are estimated using a finite element model, it is critical that the model be able to return sensible strain values that are consistent with published literature. Strains were tracked in the posterior region of human sclera globe samples from 5 mmHg (treated as the zero state) to 40 mmHg [134]. The tensile strains were found to be mostly between 1-2% in each of the 20 cases, with one case showing strains over 3%. The study used dissected partial globes that were affixed to inflate the posterior hemisphere of sclera, a case that can be compared readily to the models outlined in this work. Girard et al. performed another study using the same hemisphere inflation method, reporting maximum principal strains for each of 4 porcine globes between 2-3% at 20 mmHg [135]. Another work by Wong et al. investigated the strains of the porcine posterior sclera of genipin-treated and untreated whole globes using strain markers [119]. This particular study is of obvious interest to us due to their use of the same cross-linking agent. The group reported strains of between 0.5-1% for the untreated globe posterior regions at 20 mmHg depending on the direction. For the genipin samples, direction was seen not to matter as much, with both directional strains around 0.2% at 20 mmHg. These strains align nicely with those modeled in this work, comparing our control material model strains at 18 mmHg of 0.8-1.3% to our genipin material model strain of 0.07% at the same pressure. Still another work by MJA Girard et al. extracted principal strains from a set of eight rhesus monkey eyes [93]. The reported principal strains were measured via displacement tracking using the familiar fixed-hemisphere setup from their other works, and a material model for FE simulation was created using those displacements to inform a differential evolution algorithm. The

measured strains were measured at 10 and 30 mmHg, allowing for linear interpolation to approximate the principal strain at 20 mmHg. The estimated average principal strain in the young eyes was 0.59%, and 0.27% in the old group. These strains are noted to be low across all samples by the author, and the fact they were recorded from rhesus monkey globes likely plays a role as well. This group's material model focused on the un-crimping of collagen fibers within the tissue, and they were able to model the measured displacements well.

A different study used 3-D digital image correlation to track the strains of a 98-year old human globe sample, also dissected and affixed to study the posterior hemisphere [136]. This study was able to measure strains in the circumferential and meridional directions, and at pressure steps of 5-15 mmHg. A maximum circumferential strain of 1.8% and a minimum circumferential strain of -1.5% were reported. The maximum and minimum meridional strains were 4.1% and -1.1%, respectively. These strains are consistent with our reported strains of 1.3% and 0.8% for the free surface in the principal planar directions, although the reported strains are measured in the peripapillary region of the eye. It should be noted that all the previously published experimental results cited here are for the posterior region of the eye which is known to be less stiff than the perilimbal sclera[99], as modeled in the current work.

6.5.2 Limitation of the FE Models

There are limitations to the conclusions that can be drawn from the material model and sphere segment FE model in our study. It was necessary for us to extract tensile material properties from dogbone material samples, and this causes a number of challenges in relating the material model back to the *in vivo* globe condition. We treated our tensile dogbone samples carefully, working quickly after the globes had been enucleated and controlling their environment with the hopes of testing tissue that was analogous to the *in vivo* condition. However, there is undoubtedly something lost between the live specimen and its evaluation with excised specimens 24h post globe enucleation. As highlighted earlier in the document, properties extracted from uniaxial tensile tests will necessarily lose some of the complexity of the whole-tissue response. In this case, it appears that our material model has done a quality job in capturing the necessary material properties to describe spherical tissue strains based on IOP-analogous loading. Still, some nuance

is likely missing, and it cannot be stated under what conditions this model may fail to replicate the modeled IOP perfusion process.

This FE model (along with the eighth sphere validation model) was constructed as a segment of a perfect sphere. It is known that the eye is approximately spherical, but exhibits variance in its sphericity as a prolate or oblate spheroid depending on the specimen [137]. Further, there is a deviation in sphericity from the sclera to the cornea. The porcine globes that were inflated or dissected in the course of this work were consistently noted to have a more significant deviation from sphericity than the few human specimens examined. The location of the aqueous veins within the sclera causes another problem in this model. In the FE model in this work the vein was located in the middle of the thickness of the sclera (approx. 750 μm), and it was modeled with a diameter of 100 μm . The aqueous venous plexuses in humans have been measured at a depth within the tissue of between 100 and 350 μm [34], although components of the aqueous outflow pathway have been imaged at depths of 1000 μm [35]. Aqueous vein diameters are measured with a range from 18 to 75 μm [34]. The depth of the vein structure in this model was chosen for ease of modeling, as it had to be connected to the external ordered hexahedral element structure. However, there is clearly some value to exploring a vein structure or structures that are located at a shallower depth within the tissue segment, and aqueous veins are generally located shallower than the modeled vein. The vein diameter was modeled as 100 μm internal diameter to preserve a reasonable minimum element size, where smaller elements would only increase the FE model runtime. The FE material model was already a computational burden, and so any possible runtime optimizations were implemented to allow ease of experimentation. Another similar point here is that the vein elements were modeled as linear elastic to simplify their runtime impact. There was no fluid structure interaction model used in this work, both due to model runtime considerations and to the theoretical complexity involved in such an undertaking and is beyond the scope of this thesis. It is possible that a 2D “slice” model of the chunk model in this work, constructed of shell elements with the same prescribed symmetry and IOP boundary conditions, could be an appropriate simplification of the model to allow for shorter runtimes while giving an idea of the system response.

The model also does not consider any sort of boundary conditions on the outer surface of the tissue that would be related to the surrounding vascular, adipose, muscular, or bone tissue *in vivo*. The LaPlace law for stress in a thin-walled spherical structure is an effective estimator of the stress in the in-plane directions of this model, but it is known that it is not an appropriate model for a non-spherical and heterogeneous structure such as the eye globe, nor is it appropriate to assume the stress in the entire sphere wall is uniform [138]. In mentioning heterogeneity, it is also noted that, in addition to being isotropic, the material model used for the chunk model in this work is also homogeneous, other than in the vicinity of the vein. Although this work was not overly concerned with directional variation of properties, any work that sought to build on this and comment on the distribution of collagen within the tissue would require a different material model. There is always some nuance that is lost with the choice and application of a material model in FE studies. This is simply the nature of using a model to describe a natural phenomenon. There would have been similarly identifiable flaws in any of the candidate material models, and we believe that the one chosen for this work was as sufficient as any other may have been in this application.

In summary, we have demonstrated the strong stiffening effect of genipin crosslinker at 0.5 and 10 mm/min strain rates. These results book-end much of the quasi-static regime at which tensile eye tissue experiments are performed, and generally show a good agreement with those of published data. The strong significance of the tangent modulus at both 0.5 and 10 mm/min demonstrates an effect from the crosslinking agent that is still visible within the linear region of tissue. The significance of the stress at 8% strain from the 0.5 mm/min data is consistent with other reports mentioned above. The disappearance of significance with the 100 mm/min data suggests that high rate effects dominate the tissue elastic behavior in that regime. However, there is strong evidence from the 5-parameter model results that the behavior of the tissue at 100 mm/min loading rate in stress relaxation is altered by the genipin treatment.

Chapter 7: Conclusions

This thesis considers the structural mechanical behavior of porcine sclera tissue by using uniaxial tensile test data, optimized FE material models, and FE models of uniaxial tensile samples and Whole-Globe regions of sclera with a single embedded vein structure. A crosslinking agent was used to successfully alter the properties of the tissue samples in a measurable way. The genipin crosslinked tissues were found to be stiffer in several different measures than their untreated counterparts, both in 8% stress, tangent modulus, and stress relaxation behavior. The tensile test data collected from those experiments was used as an input for an optimization routine that was able to identify best-fit material model parameters for different material and loading cases. The material parameters found in those cases were reflective of the differences between the crosslinked and control tissues. Those material parameters were then used to inform the stress-strain relationship in FE models of sclera tissue under different forms of loading, both uniaxial tension and IOP loading. The FE models simulating the perfusion IOP stresses on the eye were able to generate strains that are consistent both with other FE models of similar processes and with strain data collected from imaging of various partial and whole inflated globes. In doing this, a technique has been established by which any of a wide range of input data can theoretically be collected and used to train a FE material model that can then be implemented to predict soft tissue response behavior in a FE model.

Funding

This thesis is based upon work supported by the Nation Science Foundation under grant number CMMI-1760291. This support is gratefully acknowledged. Any opinions, findings, conclusions, or recommendations expressed in this material are those of the author and do not necessarily reflect the views of the National Science Foundation.

Appendix 1

Excel functions used to separate relaxation data. These functions are all calibrated to work with the “Data” sheet as it currently exists to process the output data from the uniaxial tensile testing machine.

SHEETNAME: the name of the sheet as printed on the tab at the bottom of the excel document.

CELL_ID: any cell ID given by letter/number combination, e.g. H8

1. MAX(SHEETNAME!CELL_ID_1:CELL_ID_2)

Located in the first function column. Occupies one cell. This is CELL_ID_3.

CELL_ID_1 and CELL_ID_2 are the first and last cells of the column of stress data.

This function will identify the maximum value in a set of data. Here it is used to identify that maximum stress achieved by the input data.

2. ADDRESS((MATCH(CELL_ID_3,SHEETNAME!CELL_ID_1:CELL_ID_2,0)+7),8,1,1,"SHEETNAME"))

Located in the second function column, which extends the length of the relaxation data. This is CELL_ID_4.

This expression is unique to all following cells in its column. It uses the MATCH function to identify the value from function 1 and print its cell ID within the cell as SHEETNAME!\$ROW\$COLUMN, e.g. Data!\$H\$3351.

3. CELL("row",(INDIRECT(CELL_ID_4)))

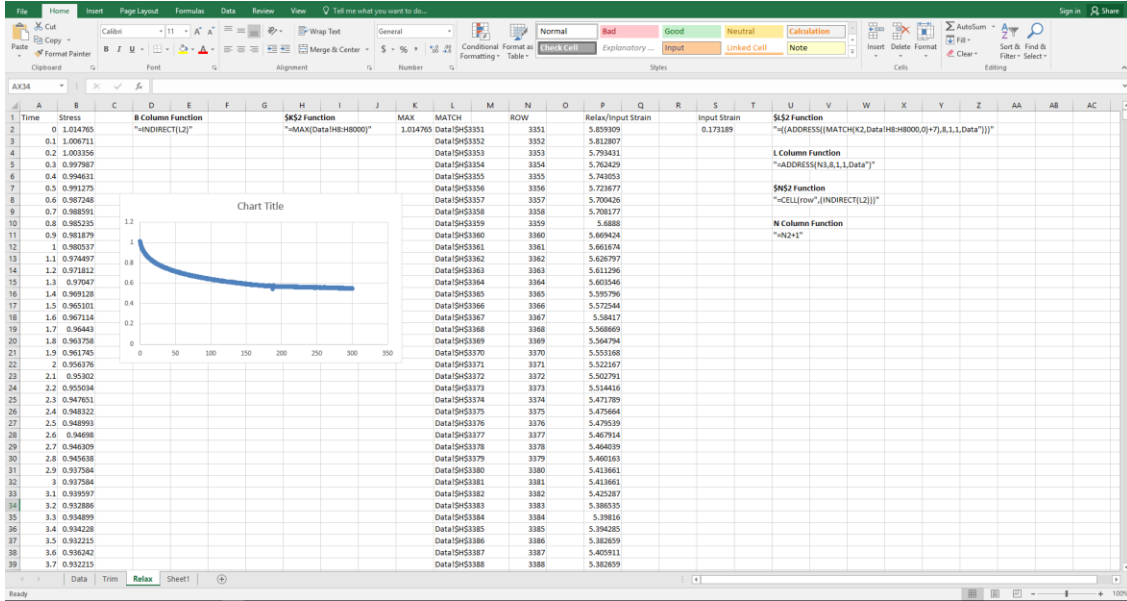
Located in the third function column. This is CELL_ID_5. This column will now print the row value associated with each cell. Using the above cell example, this function prints “3351”. The remainder of the third function column is then populated using a simple addition function (CELL_ID_5 + 1, etc.)

4. ADDRESS(CELL_ID_5,8,1,1,"SHEETNAME")

Located in the second function column, directly under function 2. This function will populate the remainder of the second function column with cell IDs of the form in function 2., e.g. Data!\$H\$3352, etc. This serves to identify the cell location of all of the data points of the relaxation portion of the curve in the second function column.

5. INDIRECT(CELL_ID_5)

This function is located in the fourth function column, and will be populated with the actual stress values of the relaxation curve. It takes the values printed in the second function column and returns the values of those cells. The functions below this one all continue to reference the cells of function 4.



References

- [1] L.v. Salvini-Plawen, On the evolution of photoreceptors and eyes, *Evol Biol* 10 (1961) 207-263.
- [2] W.J. Gehring, K. Ikeo, Pax 6: mastering eye morphogenesis and eye evolution, *Trends in genetics* 15(9) (1999) 371-377.
- [3] C. Darwin, On the origin of species: A facsimile of the first edition, Harvard University Press 1964.
- [4] T.D. Lamb, Evolution of the eye, *Scientific American* 305(1) (2011) 64-69.
- [5] I. Sanchez, R. Martin, F. Ussa, I. Fernandez-Bueno, The parameters of the porcine eyeball, *Graefe's Archive for Clinical and Experimental Ophthalmology* 249(4) (2011) 475-482.
- [6] Y. Lei, D.R. Overby, A.T. Read, W.D. Stamer, C.R. Ethier, A new method for selection of angular aqueous plexus cells from porcine eyes: a model for Schlemm's canal endothelium, *Investigative ophthalmology & visual science* 51(11) (2010) 5744-5750.
- [7] H.A. Quigley, A.T. Broman, The number of people with glaucoma worldwide in 2010 and 2020, *British Journal of Ophthalmology* 90(3) (2006) 262.
- [8] P. Boeder, Co-operative action of extra-ocular muscles, *The British journal of ophthalmology* 46(7) (1962) 397.
- [9] S.K. Ng, W. Chan, M.M. Marcet, H. Kakizaki, D. Selva, Levator palpebrae superioris: an anatomical update, *Orbit* 32(1) (2013) 76-84.
- [10] C.E. Willoughby, D. Ponzin, S. Ferrari, A. Lobo, K. Landau, Y. Omid, Anatomy and physiology of the human eye: effects of mucopolysaccharidoses disease on structure and function—a review, *Clinical & Experimental Ophthalmology* 38 (2010) 2-11.
- [11] M.S. Sridhar, Anatomy of cornea and ocular surface, *Indian journal of ophthalmology* 66(2) (2018) 190.
- [12] B.S. Shaheen, M. Bakir, S. Jain, Corneal nerves in health and disease, *Survey of ophthalmology* 59(3) (2014) 263-285.

- [13] E.M. Van Buskirk, The anatomy of the limbus, *Eye* 3(2) (1989) 101-108.
- [14] B. Coudrillier, J. Pijanka, J. Jefferys, T. Sorensen, H.A. Quigley, C. Boote, T.D. Nguyen, Collagen structure and mechanical properties of the human sclera: analysis for the effects of age, *Journal of biomechanical engineering* 137(4) (2015) 041006-041006.
- [15] P.N. Lewis, C. Pinali, R.D. Young, K.M. Meek, A.J. Quantock, C. Knupp, Structural interactions between collagen and proteoglycans are elucidated by three-dimensional electron tomography of bovine cornea, *Structure* 18(2) (2010) 239-245.
- [16] J.A. Rada, V.R. Achen, S. Penugonda, R.W. Schmidt, B.A. Mount, Proteoglycan Composition in the Human Sclera During Growth and Aging, *Invest Ophthalmol Vis Sci* 41(7) (2000) 1639.
- [17] J.K. Pijanka, A. Abass, T. Sorensen, A. Elsheikh, C. Boote, A wide-angle X-ray fibre diffraction method for quantifying collagen orientation across large tissue areas: application to the human eyeball coat, *Journal of Applied Crystallography* 46(5) (2013) 1481-1489.
- [18] K.R. Murthy, R. Goel, Y. Subbannayya, H.K.C. Jacob, P.R. Murthy, S.S. Manda, A.H. Patil, R. Sharma, N.A. Sahasrabudhe, A. Parashar, Proteomic analysis of human vitreous humor, *Clinical proteomics* 11(1) (2014) 1-11.
- [19] D.K. Sunderland, A. Sapra, *Physiology, aqueous humor circulation*, (2020).
- [20] C. Vass, C. Hirn, E. Unger, W. Mayr, M. Georgopoulos, G. Rainer, S. Richter-Mueksch, Human aqueous humor viscosity in cataract, primary open angle glaucoma and pseudoexfoliation syndrome, *Investigative Ophthalmology & Visual Science* 45(13) (2004) 5030-5030.
- [21] M. Goel, R.G. Picciani, R.K. Lee, S.K. Bhattacharya, Aqueous humor dynamics: a review, *The open ophthalmology journal* 4 (2010) 52-59.
- [22] T. Carreon, E. van der Merwe, R.L. Fellman, M. Johnstone, S.K. Bhattacharya, Aqueous outflow-A continuum from trabecular meshwork to episcleral veins, *Progress in retinal and eye research* 57 (2017) 108-133.
- [23] A. Bill, Uveoscleral drainage of aqueous humor: physiology and pharmacology, *Progress in clinical and biological research* 312 (1989) 417-427.
- [24] A. Alm, S.F.E. Nilsson, Uveoscleral outflow – A review, *Experimental Eye Research* 88(4) (2009) 760-768.
- [25] S.F. Nilsson, The uveoscleral outflow routes, *Eye (Lond)* 11 (Pt 2) (1997) 149-54.

- [26] E.R. Tamm, The trabecular meshwork outflow pathways: Structural and functional aspects, *Experimental Eye Research* 88(4) (2009) 648-655.
- [27] E. Lütjen-Drecoll, Functional morphology of the trabecular meshwork in primate eyes, *Progress in Retinal and Eye Research* 18(1) (1999) 91-119.
- [28] K.E. Keller, M. Aga, J.M. Bradley, M.J. Kelley, T.S. Acott, Extracellular matrix turnover and outflow resistance, *Experimental Eye Research* 88(4) (2009) 676-682.
- [29] L. Kagemann, G. Wollstein, H. Ishikawa, I.A. Sigal, L.S. Folio, J. Xu, H. Gong, J.S. Schuman, 3D visualization of aqueous humor outflow structures in-situ in humans, *Experimental Eye Research* 93(3) (2011) 308-315.
- [30] M.D. Bentley, C.R. Hann, M.P. Fautsch, Anatomical Variation of Human Collector Channel Orifices, *Investigative Ophthalmology & Visual Science* 57(3) (2016) 1153-1159.
- [31] C. Xin, R.K. Wang, S. Song, T. Shen, J. Wen, E. Martin, Y. Jiang, S. Padilla, M. Johnstone, Aqueous outflow regulation: Optical coherence tomography implicates pressure-dependent tissue motion, *Experimental eye research* 158 (2017) 171-186.
- [32] J.M. Ramírez, A.I. Ramírez, J.J. Salazar, B. Rojas, R. De Hoz, A. Triviño, Schlemm's canal and the collector channels at different developmental stages in the human eye, *Cells Tissues Organs* 178(3) (2004) 180-185.
- [33] H. Gong, A. Francis, Schlemm's Canal and Collector Channels as Therapeutic Targets, in: J.R. Samples, I.I.K. Ahmed (Eds.), *Surgical Innovations in Glaucoma*, Springer New York, New York, NY, 2014, pp. 3-25.
- [34] L. Kagemann, G. Wollstein, H. Ishikawa, Z. Nadler, I.A. Sigal, L.S. Folio, J.S. Schuman, Visualization of the Conventional Outflow Pathway in the Living Human Eye, *Ophthalmology* 119(8) (2012) 1563-1568.
- [35] T. Akagi, A. Uji, A.S. Huang, R.N. Weinreb, T. Yamada, M. Miyata, T. Kameda, H.O. Ikeda, A. Tsujikawa, Conjunctival and Intrascleral Vasculatures Assessed Using Anterior Segment Optical Coherence Tomography Angiography in Normal Eyes, *American Journal of Ophthalmology* 196 (2018) 1-9.
- [36] Y.-c. Fung, *Biomechanics: mechanical properties of living tissues*, Springer Science & Business Media 1993.
- [37] A.M. Taylor, B. Bordoni, Histology, blood vascular system, StatPearls [Internet] (2020).

- [38] M. Abovsky, Y. Lanir, E. Nevo, Tethering affects the mechanics of coronary capillaries, *J Biomech* 29(5) (1996) 597-607.
- [39] M.J. Hogan, *Histology of the human eye, An atlas and textbook* (1971).
- [40] F.A. Jakobiec, *Ocular anatomy, embryology, and teratology*, Harpercollins1982.
- [41] H. Davson, *Physiology of the Eye*, Bloomsbury Publishing1990.
- [42] J.L. Wiggs, L.R. Pasquale, Genetics of glaucoma, *Human Molecular Genetics* 26(R1) (2017) R21-R27.
- [43] R.N. Weinreb, T. Aung, F.A. Medeiros, *The Pathophysiology and Treatment of Glaucoma: A Review*, *JAMA* 311(18) (2014) 1901-1911.
- [44] J. Chua, M. Baskaran, P.G. Ong, Y. Zheng, T.Y. Wong, T. Aung, C.-Y. Cheng, Prevalence, Risk Factors, and Visual Features of Undiagnosed Glaucoma: The Singapore Epidemiology of Eye Diseases Study, *JAMA Ophthalmology* 133(8) (2015) 938-946.
- [45] R.N. Weinreb, P.T. Khaw, Primary open-angle glaucoma, *The Lancet* 363(9422) (2004) 1711-1720.
- [46] Y.-C. Tham, X. Li, T.Y. Wong, H.A. Quigley, T. Aung, C.-Y. Cheng, Global Prevalence of Glaucoma and Projections of Glaucoma Burden through 2040: A Systematic Review and Meta-Analysis, *Ophthalmology* 121(11) (2014) 2081-2090.
- [47] E.R. Tamm, Myocilin and glaucoma: facts and ideas, *Prog Retin Eye Res* 21(4) (2002) 395-428.
- [48] W.L.M. Alward, The genetics of open-angle glaucoma: The story of *GLC1A* and myocilin, *Eye* 14(3) (2000) 429-436.
- [49] Z.T. Resch, M.P. Fautsch, Glaucoma-associated myocilin: A better understanding but much more to learn, *Experimental Eye Research* 88(4) (2009) 704-712.
- [50] E.K. de Jong, M.J. Geerlings, A.I. den Hollander, Age-related macular degeneration, *Genetics and genomics of eye disease* (2020) 155-180.
- [51] R.D. Jager, W.F. Mieler, J.W. Miller, Age-related macular degeneration, *New England Journal of Medicine* 358(24) (2008) 2606-2617.
- [52] K.N. Khan, O.A. Mahroo, R.S. Khan, M.D. Mohamed, M. McKibbin, A. Bird, M. Michaelides, A. Tufail, A.T. Moore, Differentiating drusen: Drusen and drusen-like appearances associated with ageing, age-related macular degeneration, inherited eye disease and other pathological processes, *Progress in retinal and eye research* 53 (2016) 70-106.

- [53] X. Ding, M. Patel, C.-C. Chan, Molecular pathology of age-related macular degeneration, *Progress in retinal and eye research* 28(1) (2009) 1-18.
- [54] A.R. Rudnicka, Z. Jarrar, R. Wormald, D.G. Cook, A. Fletcher, C.G. Owen, Age and gender variations in age-related macular degeneration prevalence in populations of European ancestry: a meta-analysis, *Ophthalmology* 119(3) (2012) 571-580.
- [55] E. Friedman, M. Ivry, E. Ebert, R. Glynn, E. Gragoudas, J. Seddon, Increased scleral rigidity and age-related macular degeneration, *Ophthalmology* 96(1) (1989) 104-108.
- [56] I.G. Pallikaris, G.D. Kymionis, H.S. Ginis, G.A. Kounis, E. Christodoulakis, M.K. Tsilimbaris, Ocular rigidity in patients with age-related macular degeneration, *American journal of ophthalmology* 141(4) (2006) 611-611.
- [57] B. Coudrillier, J.K. Pijanka, J.L. Jefferys, A. Goel, H.A. Quigley, C. Boote, T.D. Nguyen, Glaucoma-related changes in the mechanical properties and collagen micro-architecture of the human sclera, *PLoS One* 10(7) (2015) e0131396.
- [58] P.M. Pinsky, D. van der Heide, D. Chernyak, Computational modeling of mechanical anisotropy in the cornea and sclera, *J Cataract Refract Surg* 31(1) (2005) 136-145.
- [59] R. Grytz, M.A. Fazio, M.J.A. Girard, V. Libertiaux, L. Bruno, S. Gardiner, C.A. Girkin, J. Crawford Downs, Material properties of the posterior human sclera, *Journal of the Mechanical Behavior of Biomedical Materials* 29 (2014) 602-617.
- [60] B. Wang, Y. Hua, B.L. Brazile, B. Yang, I.A. Sigal, Collagen fiber interweaving is central to sclera stiffness, *Acta Biomaterialia* 113 (2020) 429-437.
- [61] J.A. Bisplinghoff, C. McNally, S.J. Manoogian, S.M. Duma, Dynamic material properties of the human sclera, *J Biomech* 42(10) (2009) 1493-1497.
- [62] R.E. Norman, J.G. Flanagan, I.A. Sigal, S.M.K. Rausch, I. Tertinegg, C.R. Ethier, Finite element modeling of the human sclera: influence on optic nerve head biomechanics and connections with glaucoma, *Exp Eye Res* 93(1) (2011) 4.
- [63] D.R. Lari, D.S. Schultz, A.S. Wang, O.-T. Lee, J.M. Stewart, Scleral mechanics: comparing whole globe inflation and uniaxial testing, *Exp Eye Res* 94(1) (2012) 128.
- [64] G.A. Holzapfel, Biomechanics of soft tissue, *The handbook of materials behavior models* 3(1) (2001) 1049-1063.
- [65] R.W. Ogden, Nonlinear elasticity, anisotropy, material stability and residual stresses in soft tissue, *Biomechanics of soft tissue in cardiovascular systems*, Springer2003, pp. 65-108.

- [66] J.A. Weiss, B.N. Maker, S. Govindjee, Finite element implementation of incompressible, transversely isotropic hyperelasticity, *Computer methods in applied mechanics and engineering* 135(1-2) (1996) 107-128.
- [67] A. Chawla, S. Mukherjee, R. Marathe, B. Karthikeyan, R. Malhotra, Determining strain rate dependence of human body soft tissues using a split Hopkinson pressure bar, pp. 20-22.
- [68] W. Kim, A. Argento, F.W. Rozsa, K. Mallett, Constitutive behavior of ocular tissues over a range of strain rates, *Journal of biomechanical engineering* 134(6) (2012).
- [69] B. Zhou, F. Xu, C.Q. Chen, T.J. Lu, Strain rate sensitivity of skin tissue under thermomechanical loading, *Philosophical Transactions of the Royal Society A: Mathematical, Physical and Engineering Sciences* 368(1912) (2010) 679-690.
- [70] M. Righi, V. Balbi, *Foundations of Viscoelasticity and Application to Soft Tissue Mechanics, Modeling Biomaterials*, Springer2021, pp. 71-103.
- [71] Z.L. Shen, H. Kahn, R. Ballarini, S.J. Eppell, Viscoelastic properties of isolated collagen fibrils, *Biophysical journal* 100(12) (2011) 3008-3015.
- [72] A. Serra-Aguila, J. Puigoriol-Forcada, G. Reyes, J. Menacho, Viscoelastic models revisited: Characteristics and interconversion formulas for generalized Kelvin–Voigt and Maxwell models, *Acta Mechanica Sinica* 35(6) (2019) 1191-1209.
- [73] D.H. Glass, C.J. Roberts, A.S. Litsky, P.A. Weber, A viscoelastic biomechanical model of the cornea describing the effect of viscosity and elasticity on hysteresis, *Investigative ophthalmology & visual science* 49(9) (2008) 3919-3926.
- [74] A. Viidik, A rheological model for uncalcified parallel-fibred collagenous tissue, *Journal of Biomechanics* 1(1) (1968) 3-11.
- [75] N.-J. Jan, C. Gomez, S. Moed, A.P. Voorhees, J.S. Schuman, R.A. Bilonick, I.A. Sigal, Microstructural crimp of the lamina cribrosa and peripapillary sclera collagen fibers, *Investigative ophthalmology & visual science* 58(9) (2017) 3378-3388.
- [76] Y. He, Y. Guo, J. Wang, W. Lv, X. Li, K. Chen, The posterior eye with age-related macular degeneration has isotropic and nonlinear viscoelastic properties, *Journal of the Mechanical Behavior of Biomedical Materials* 114 (2021) 104207.
- [77] A.H.-D. Cheng, *Poroelasticity*, Springer2016.
- [78] I.A. Stokes, S. Chegini, S.J. Ferguson, M.G. Gardner-Morse, J.C. Iatridis, J.P. Laible, Limitation of finite element analysis of poroelastic behavior of biological tissues undergoing rapid loading, *Annals of biomedical engineering* 38(5) (2010) 1780-1788.

- [79] K.L. Troyer, C.M. Puttlitz, Human cervical spine ligaments exhibit fully nonlinear viscoelastic behavior, *Acta Biomaterialia* 7(2) (2011) 700-709.
- [80] C. Untaroiu, K. Darvish, J. Crandall, B. Deng, J.-T. Wang, *A Finite Element Model of the Lower Limb for Simulating Pedestrian Impacts*, The Stapp Association, 2005.
- [81] L.S.D.K.U.s. Manual, vol. II, Livermore Software Technology Corporation (LSTC) (2013).
- [82] M.E. Taylor, K.E. Tanner, M.A.R. Freeman, A.L. Yettram, Stress and strain distribution within the intact femur: compression or bending?, *Medical engineering & physics* 18(2) (1996) 122-131.
- [83] C.E. Henning, M.A. Lynch, K.R. Glick Jr, An in vivo strain gage study of elongation of the anterior cruciate ligament, *The American journal of sports medicine* 13(1) (1985) 22-26.
- [84] A. Grinbaum, M. Blumenthal, E. Assia, Comparison of intraocular pressure profiles during cataract surgery by phacoemulsification and extracapsular cataract extraction, *Slack Incorporated Thorofare, NJ*, 2003, pp. 182-186.
- [85] Y. Zhao, X. Li, A. Tao, J. Wang, F. Lu, Intraocular pressure and calculated diastolic ocular perfusion pressure during three simulated steps of phacoemulsification in vivo, *Investigative ophthalmology & visual science* 50(6) (2009) 2927-2931.
- [86] A. Bill, C.I. Phillips, Uveoscleral drainage of aqueous humour in human eyes, *Experimental eye research* 12(3) (1971) 275-281.
- [87] B. Becker, M.A. Constant, The facility of aqueous outflow: A comparison of tonography and perfusion measurements in vivo and in vitro, *AMA archives of ophthalmology* 55(3) (1956) 305-312.
- [88] Z. Zhi, W. Cepurna, E. Johnson, H. Jayaram, J. Morrison, R.K. Wang, Evaluation of the effect of elevated intraocular pressure and reduced ocular perfusion pressure on retinal capillary bed filling and total retinal blood flow in rats by OMAG/OCT, *Microvascular research* 101 (2015) 86-95.
- [89] J.S. Schuman, K. Erickson, J.A. Nathanson, Nitrovasodilator effects on intraocular pressure and outflow facility in monkeys, *Experimental eye research* 58(1) (1994) 99-105.
- [90] S. Takai, S.L.Y. Woo, G.A. Livesay, D.J. Adams, F.H. Fu, Determination of the in situ loads on the human anterior cruciate ligament, *Journal of Orthopaedic Research* 11(5) (1993) 686-695.
- [91] P.R. Greene, T.A. McMahon, Scleral creep vs. temperature and pressure in vitro, *Experimental eye research* 29(5) (1979) 527-537.

- [92] M.J.A. Girard, J.C. Downs, M. Bottlang, C.F. Burgoyne, J.K.F. Suh, Peripapillary and Posterior Scleral Mechanics—Part II: Experimental and Inverse Finite Element Characterization, *Journal of Biomechanical Engineering* 131(5) (2009).
- [93] M.J.A. Girard, J.K.F. Suh, M. Bottlang, C.F. Burgoyne, J.C. Downs, Scleral Biomechanics in the Aging Monkey Eye, *Investigative Ophthalmology & Visual Science* 50(11) (2009) 5226-5237.
- [94] C. Nguyen, F.E. Cone, T.D. Nguyen, B. Coudrillier, M.E. Pease, M.R. Steinhart, E.N. Oglesby, J.L. Jefferys, H.A. Quigley, Studies of scleral biomechanical behavior related to susceptibility for retinal ganglion cell loss in experimental mouse glaucoma, *Investigative ophthalmology & visual science* 54(3) (2013) 1767-1780.
- [95] B. Coudrillier, J. Tian, S. Alexander, K.M. Myers, H.A. Quigley, T.D. Nguyen, Biomechanics of the human posterior sclera: age- and glaucoma-related changes measured using inflation testing, *Invest Ophthalmol Vis Sci* 53(4) (2012) 1714.
- [96] P.A. Scott, Z. Lu, Y. Liu, H. Gong, Relationships between increased aqueous outflow facility during washout with the changes in hydrodynamic pattern and morphology in bovine aqueous outflow pathways, *Experimental eye research* 89(6) (2009) 942-949.
- [97] K.S. Hunter, T. Fjield, H. Heitzmann, R. Shandas, M.Y. Kahook, Characterization of micro-invasive trabecular bypass stents by ex vivo perfusion and computational flow modeling, *Clinical Ophthalmology (Auckland, NZ)* 8 (2014) 499.
- [98] L.J. Camras, F. Yuan, S. Fan, T.W. Samuelson, I.K. Ahmed, A.T. Schieber, C.B. Toris, A novel Schlemm's Canal scaffold increases outflow facility in a human anterior segment perfusion model, *Invest Ophthalmol Vis Sci* 53(10) (2012) 6115.
- [99] X. Man, E. Arroyo, M. Dunbar, D.M. Reed, N. Shah, L. Kagemann, W. Kim, S.E. Moroi, A. Argento, Perilimbal sclera mechanical properties: Impact on intraocular pressure in porcine eyes, *PLOS ONE* 13(5) (2018) e0195882.
- [100] L. Ni, J. Riesterer, H. Wang, L. Berry, K. Blackburn, J. Chuang, W. Kim, G. Xu, S.E. Moroi, A. Argento, Method for the biomechanical analysis of aqueous veins and perilimbal sclera by three-dimensional photoacoustic imaging and strain field calculation, *Scientific reports* 11(1) (2021) 1-10.
- [101] D.M. Brown, M.T. Pardue, C.R. Ethier, A biphasic approach for characterizing tensile, compressive and hydraulic properties of the sclera, *Journal of The Royal Society Interface* 18(174) (2021) 20200634.

- [102] A.M. Mortazavi, B.R. Simon, W.D. Stamer, J.P.V. Geest, Drained secant modulus for human and porcine peripapillary sclera using unconfined compression testing, *Experimental eye research* 89(6) (2009) 892-897.
- [103] A. Elsheikh, B. Geraghty, D. Alhasso, J. Knappett, M. Campanelli, P. Rama, Regional variation in the biomechanical properties of the human sclera, *Experimental Eye Research* 90(5) (2010) 624-633.
- [104] H. Hatami-Marbini, A. Rahimi, Collagen cross-linking treatment effects on corneal dynamic biomechanical properties, *Experimental Eye Research* 135 (2015) 88-92.
- [105] H. Hatami-Marbini, M. Pachenari, The contribution of sGAGs to stress-controlled tensile response of posterior porcine sclera, *Plos one* 15(2) (2020) e0227856.
- [106] D.S. Schultz, J.C. Lotz, S.M. Lee, M.L. Trinidad, J.M. Stewart, Structural Factors That Mediate Scleral Stiffness, *Investigative Ophthalmology & Visual Science* 49(10) (2008) 4232-4236.
- [107] H. Hatami-Marbini, M. Pachenari, Tensile Viscoelastic Properties of the Sclera after Glycosaminoglycan Depletion, *Current Eye Research* 46(9) (2021) 1299-1308.
- [108] M. Girard, J.-K.F. Suh, R.T. Hart, C.F. Burgoyne, J.C. Downs, Effects of Storage Time on the Mechanical Properties of Rabbit Peripapillary Sclera After Enucleation, *Curr Eye Res* 32(5) (2007) 465.
- [109] J.C. Downs, J.K.F. Suh, K.A. Thomas, A.J. Bellezza, C.F. Burgoyne, R.T. Hart, Viscoelastic Characterization of Peripapillary Sclera: Material Properties by Quadrant in Rabbit and Monkey Eyes, *J Biomech Eng* 125(1) (2003) 124-131.
- [110] A. Haneef, R.O.G. Gopalan, D.T. Rajendran, J. Nunes, D. Kuppamuthu, N. Radhakrishnan, T.-H. Young, H.-Y. Hsieh, N.V. Prajna, C.E. Willoughby, Chemical Cross-Linking of Corneal Tissue to Reduce Progression of Loss of Sight in Patients With Keratoconus, *Translational vision science & technology* 10(5) (2021) 6-6.
- [111] B.C. Perez, J. Tang, H.J. Morris, J.R. Palko, X. Pan, R.T. Hart, J. Liu, Biaxial mechanical testing of posterior sclera using high-resolution ultrasound speckle tracking for strain measurements, *Journal of biomechanics* 47(5) (2014) 1151-1156.
- [112] A. Eilaghi, J.G. Flanagan, I. Tertinegg, C.A. Simmons, G. Wayne Brodland, C. Ross Ethier, Biaxial mechanical testing of human sclera, *Journal of Biomechanics* 43(9) (2010) 1696-1701.

- [113] H. Lei, L.A. Johnson, K.A. Eaton, S. Liu, J. Ni, X. Wang, P.D.R. Higgins, G. Xu, Characterizing intestinal strictures of Crohn's disease in vivo by endoscopic photoacoustic imaging, *Biomed. Opt. Express* 10(5) (2019) 2542-2555.
- [114] F. Stan, C. Fetecau, Study of stress relaxation in polytetrafluoroethylene composites by cylindrical macroindentation, *Composites Part B: Engineering* 47 (2013) 298-307.
- [115] T.R. Friberg, J.W. Lace, A comparison of the elastic properties of human choroid and sclera, *Exp Eye Res* 47(3) (1988) 429-436.
- [116] M. Yamanari, K. Ishii, S. Fukuda, Y. Lim, L. Duan, S. Makita, M. Miura, T. Oshika, Y. Yasuno, Optical rheology of porcine sclera by birefringence imaging, (2012).
- [117] J. Park, A. Shin, S. Jafari, J.L. Demer, Material properties and effect of preconditioning of human sclera, optic nerve, and optic nerve sheath, *Biomechanics and Modeling in Mechanobiology* 20(4) (2021) 1353-1363.
- [118] A. Elsheikh, W. Kassem, S.W. Jones, Strain-rate sensitivity of porcine and ovine corneas, *Acta Bioeng Biomech* 13(2) (2011) 25-36.
- [119] F.F. Wong, D.R. Lari, D.S. Schultz, J.M. Stewart, Whole globe inflation testing of exogenously crosslinked sclera using genipin and methylglyoxal, *Exp Eye Res* 103 (2012) 17.
- [120] K. Adamiak, A. Sionkowska, Current methods of collagen cross-linking: Review, *International Journal of Biological Macromolecules* 161 (2020) 550-560.
- [121] G. Wollensak, E. Spoerl, Collagen crosslinking of human and porcine sclera, *Journal of Cataract & Refractive Surgery* 30(3) (2004) 689-695.
- [122] G. Wollensak, E. Iomdina, Long-term biomechanical properties of rabbit sclera after collagen crosslinking using riboflavin and ultraviolet A (UVA), *Acta ophthalmologica* 87(2) (2009) 193-198.
- [123] T.-X. Liu, Z. Wang, Biomechanics of sclera crosslinked using genipin in rabbit, *International journal of ophthalmology* 10(3) (2017) 355.
- [124] T.X. Liu, Z. Wang, Collagen crosslinking of porcine sclera using genipin, *Acta ophthalmologica* 91(4) (2013) e253-e257.
- [125] B. Xu, H. Li, Y. Zhang, Understanding the viscoelastic behavior of collagen matrices through relaxation time distribution spectrum, *Biomatter* 3(3) (2013) e24651.

- [126] J.C. Downs, J.K.F. Suh, K.A. Thomas, A.J. Bellezza, R.T. Hart, C.F. Burgoyne, Viscoelastic material properties of the peripapillary sclera in normal and early-glaucoma monkey eyes, *Investigative ophthalmology & visual science* 46(2) (2005) 540-546.
- [127] C. Untaroiu, K. Darvish, J. Crandall, B. Deng, J.-T. Wang, Characterization of the lower limb soft tissues in pedestrian finite element models.
- [128] G.G. Wang, S. Shan, Review of Metamodeling Techniques in Support of Engineering Design Optimization, *Journal of Mechanical Design* 129(4) (2006) 370-380.
- [129] R.R. Barton, M. Meckesheimer, Metamodel-based simulation optimization, *Handbooks in operations research and management science* 13 (2006) 535-574.
- [130] S.A. Schwaner, B.G. Hannon, A.J. Feola, C.R. Ethier, Biomechanical properties of the rat sclera obtained with inverse finite element modeling, *Biomechanics and Modeling in Mechanobiology* 19(6) (2020) 2195-2212.
- [131] C. Lanczos, *Applied analysis*, Courier Corporation 1988.
- [132] D.R. Einstein, A.D. Freed, N. Stander, B. Fata, I. Vesely, Inverse parameter fitting of biological tissues: a response surface approach, *Annals of Biomedical Engineering* 33(12) (2005) 1819-1830.
- [133] D.A. Atchison, G. Smith, *Optics of the human eye*, Butterworth-Heinemann Oxford 2000.
- [134] M.A. Fazio, R. Grytz, L. Bruno, M.J.A. Girard, S. Gardiner, C.A. Girkin, J.C. Downs, Regional Variations in Mechanical Strain in the Posterior Human Sclera, *Invest Ophthalmol Vis Sci* 53(9) (2012) 5326-5333.
- [135] M.J.A. Girard, J.C. Downs, C.F. Burgoyne, J.K.F. Suh, Experimental surface strain mapping of porcine peripapillary sclera due to elevations of intraocular pressure, *Journal of biomechanical engineering* 130(4) (2008).
- [136] J.D. Pyne, K. Genovese, L. Casaletto, J.P. Vande Geest, Sequential-digital image correlation for mapping human posterior sclera and optic nerve head deformation, *Journal of biomechanical engineering* 136(2) (2014) 021002.
- [137] K.D. Singh, N.S. Logan, B. Gilmartin, Three-dimensional modeling of the human eye based on magnetic resonance imaging, *Investigative ophthalmology & visual science* 47(6) (2006) 2272-2279.
- [138] C.W. Chung, M.J.A. Girard, N.-J. Jan, I.A. Sigal, Use and misuse of Laplace's law in ophthalmology, *Investigative ophthalmology & visual science* 57(1) (2016) 236-245.